

Technical Report 1668

August 1994

**Surface and Upper-Air Meteorological
Measurements Supporting the
NATO/AC243/Panel 3 Research Study
Groups 8 and 21 Campaign in
Lorient, France (September 1993)**

Kenneth D. Anderson

EXECUTIVE SUMMARY

OBJECTIVE

The objective is to document and analyze two weeks of surface and upper-air meteorological measurements made in support of an international effort, coordinated by the NATO/AC23/Panel 3 Research Study Groups 8 and 21, to assess the effects of the lower atmosphere on the propagation of an electromagnetic phase front at frequencies from 10 to 94 GHz.

RESULTS

Surface and upper-air meteorological measurements were made at Gavres, France (47.42 N, 3.2 W). A total of 20 radiosondes were launched on seven different days. In all cases, the dominant propagation phenomenon was the evaporation duct.

RECOMMENDATION

It is strongly recommended that phase-front angle-of-arrival estimates calculated from surface meteorological conditions be compared to measured values.

CONCLUSIONS

The numerical modeling of propagation from waveguide theory at 10.5 and 35 GHz in normal and ducting environments indicates that the evaporation duct can raise the angle-of-arrival from about 1.5 mrad to about 6.2 mrad. In addition, surface roughness, at least on short propagation paths, has little or no effect on angle-of-arrival.

CONTENTS

EXECUTIVE SUMMARY	iii
INTRODUCTION	1
MEASUREMENT PROGRAM	2
OVERVIEW	2
METEOROLOGICAL MODEL OF THE SURFACE LAYER	4
RESULTS	7
METEOROLOGICAL MEASUREMENTS	7
ANGLE-OF-ARRIVAL ESTIMATION	8
CONCLUSIONS	9
REFERENCES	10
INITIAL DISTRIBUTION	33

FIGURES

1. The geographical region around Lorient, France, in the Bay of Biscay	11
2. Vertical profiles of the modified refractivity measured by upper-air radiosondes and surface layer calculations for 15 September 1993, 0730 GMT.	11
3. Vertical profiles of the modified refractivity measured by upper-air radiosondes and surface layer calculations for 15 September 1993, 1730 GMT.	12
4. Vertical profiles of the modified refractivity measured by upper-air radiosondes and surface layer calculations for 16 September 1993, 0715 GMT.	12
5. Vertical profiles of the modified refractivity measured by upper-air radiosondes and surface layer calculations for 16 September 1993, 1100 GMT.	13
6. Vertical profiles of the modified refractivity measured by upper-air radiosondes and surface layer calculations for 16 September 1993, 1415 GMT.	13
7. Vertical profiles of the modified refractivity measured by upper-air radiosondes and surface layer calculations for 17 September 1993, 0715 GMT.	14
8. Vertical profiles of the modified refractivity measured by upper-air radiosondes and surface layer calculations for 17 September 1993, 1115 GMT.	14
9. Vertical profiles of the modified refractivity measured by upper-air radiosondes and surface layer calculations for 17 September 1993, 1130 GMT.	15
10. Vertical profiles of the modified refractivity measured by upper-air radiosondes and surface layer calculations for 17 September 1993, 1415 GMT.	15

11. Vertical profiles of the modified refractivity measured by upper-air radiosondes and surface layer calculations for 20 September 1993, 1200 GMT.	16
12. Vertical profiles of the modified refractivity measured by upper-air radiosondes and surface layer calculations for 20 September 1993, 1430 GMT.	16
13. Vertical profiles of the modified refractivity measured by upper-air radiosondes and surface layer calculations for 21 September 1993, 0800 GMT.	17
14. Vertical profiles of the modified refractivity measured by upper-air radiosondes and surface layer calculations for 21 September 1993, 1130 GMT.	17
15. Vertical profiles of the modified refractivity measured by upper-air radiosondes and surface layer calculations for 21 September 1993, 1400 GMT.	18
16. Vertical profiles of the modified refractivity measured by upper-air radiosondes and surface layer calculations for 22 September 1993, 0700 GMT.	18
17. Vertical profiles of the modified refractivity measured by upper-air radiosondes and surface layer calculations for 22 September 1993, 0730 GMT.	19
18. Vertical profiles of the modified refractivity measured by upper-air radiosondes and surface layer calculations for 22 September 1993, 1100 GMT.	19
19. Vertical profiles of the modified refractivity measured by upper-air radiosondes and surface layer calculations for 22 September 1993, 1400 GMT.	20
20. Vertical profiles of the modified refractivity measured by upper-air radiosondes and surface layer calculations for 23 September 1993, 1130 GMT.	20
21. Vertical profiles of the modified refractivity measured by upper-air radiosondes and surface layer calculations for 23 September 1993, 1400 GMT.	21
22. Gradients of modified refractivity computed from surface layer observations and compared to gradient measured by upper-air radiosondes.	21
23. Vertical profiles of temperature, relative humidity, and modified refractivity measured by radiosondes (PP-11 processor) compared to profiles computed from surface layer observations for 15 September 1993, 0730 GMT.	22
24. Vertical profiles of the modified refractivity measured by upper-air radiosondes compared to profiles computed from surface layer observations for 15 September 1993, 1730 GMT.	22
25. Vertical profiles of the modified refractivity measured by upper-air radiosondes compared to profiles computed from surface layer observations for 16 September 1993, 0715 GMT.	23
26. Vertical profiles of the modified refractivity measured by upper-air radiosondes compared to profiles computed from surface layer observations for 16 September 1993, 1100 GMT.	23

27. Vertical profiles of the modified refractivity measured by upper-air radiosondes compared to profiles computed from surface layer observations for 16 September 1993, 1415 GMT.	24
28. Vertical profiles of the modified refractivity measured by upper-air radiosondes compared to profiles computed from surface layer observations for 17 September 1993, 0715 GMT.	24
29. Vertical profiles of the modified refractivity measured by upper-air radiosondes compared to profiles computed from surface layer observations for 17 September 1993, 1115 GMT.	25
30. Vertical profiles of the modified refractivity measured by upper-air radiosondes compared to profiles computed from surface layer observations for 17 September 1993, 1130 GMT.	25
31. Vertical profiles of the modified refractivity measured by upper-air radiosondes compared to profiles computed from surface layer observations for 17 September 1993, 1415 GMT.	26
32. Vertical profiles of the modified refractivity measured by upper-air radiosondes compared to profiles computed from surface layer observations for 20 September 1993, 1200 GMT.	26
33. Vertical profiles of the modified refractivity measured by upper-air radiosondes compared to profiles computed from surface layer observations for 20 September 1993, 1430 GMT.	27
34. Vertical profiles of the modified refractivity measured by upper-air radiosondes compared to profiles computed from surface layer observations for 21 September 1993, 0800 GMT.	27
35. Vertical profiles of the modified refractivity measured by upper-air radiosondes compared to profiles computed from surface layer observations for 21 September 1993, 1130 GMT.	28
36. Vertical profiles of the modified refractivity measured by upper-air radiosondes compared to profiles computed from surface layer observations for 21 September 1993, 1400 GMT.	28
37. Vertical profiles of the modified refractivity measured by upper-air radiosondes compared to profiles computed from surface layer observations for 22 September 1993, 0700 GMT.	29
38. Vertical profiles of the modified refractivity measured by upper-air radiosondes compared to profiles computed from surface layer observations for 22 September 1993, 0730 GMT.	29
39. Vertical profiles of the modified refractivity measured by upper-air radiosondes compared to profiles computed from surface layer observations for 22 September 1993, 1100 GMT.	30

40. Vertical profiles of the modified refractivity measured by upper-air radiosondes compared to profiles computed from surface layer observations for 22 September 1993, 1400 GMT.	30
41. Vertical profiles of the modified refractivity measured by upper-air radiosondes compared to profiles computed from surface layer observations for 23 September 1993, 1130 GMT.	31
42. Vertical profiles of the modified refractivity measured by upper-air radiosondes compared to profiles computed from surface layer observations for 23 September 1993, 1400 GMT.	31
43. Estimated angle-of-arrival at 10.5 GHz for 1130 GMT on 21 September 1993.	32
44. Estimated angle-of-arrival at 35 GHz for 1130 GMT on 21 September 1993	32

TABLES

1. List of participants.	2
2. Dates and times of radiosondes launched.	3

INTRODUCTION

The propagation of electromagnetic (EM) waves is critically dependent on atmospheric conditions. At millimeter wavelengths, one of the most well-known propagation effects is molecular absorption. It is caused by the interaction of the passing EM wave and the charge distribution of a molecule. In the troposphere, the major effects of molecular absorption are attributable to the gaseous constituents of O₂ and H₂O molecules. Although molecular absorption is generally thought to be the dominant propagation mechanism, Anderson [1990] demonstrated that the evaporation duct, a persistent propagation phenomenon over water, is capable of trapping the EM energy and guiding it along the earth's surface to ranges of more than twice the radio horizon as if there were no molecular absorption. These measurements, made at 94 GHz on a 40-km overwater path, showed that the evaporation duct typically enhanced the received signal strength by some 60 dB, which almost compensated for the loss due absorption.

At short ranges and low terminal heights, well within the radio horizon, the evaporation duct has been shown to be a significant propagation phenomenon at X-band (Dockery, 1988; Anderson, 1993). Anderson's radar measurements (*op. cit.*) clearly indicate that the vertical modified refractive index profile describing the evaporation duct must extend from the surface through the mixed layer, essentially encompassing the entire boundary layer. The refractive gradient above the surface layer has a substantial effect on propagation at moderate ranges. Typically it affects propagation from about 50% to 100% of the horizon range.

The low-altitude propagation of millimeter wavelength signals over short ranges is expected to be dominated by both absorption and evaporation ducting. Surface roughness effects (Miller, Brown, and Vegh, 1984) may also be a significant factor in the propagation of millimeter waves. For targeting and tracking systems that make use of the angle-of-arrival of a ray (direction of the normal to a wave front), ducting and surface roughness effects are of primary concern. Absorption reduces the signal strength but does not change the direction of a ray as ducting and scattering do.

The objective of a measurement and analytical effort sponsored by NATO/AC243/Panel 3 Research Study Groups 8 and 21 was to characterize surface and atmospheric effects on the propagation of EM phase fronts at millimeter wavelengths. The participants are listed in table 1. Dutch, French, and German groups provided EM transmitter and receiver systems using array or monopulse antennas to measure the angle-of-arrival. The Dutch systems (FEL/TNO) operated at 10.5 and 16 GHz; the French systems (CELAR and CERT) operated at 35 and 36 GHz; the German systems operated at 35 and 94 GHz. All five participants made surface meteorological measurements (CELAR and FEL/TNO had buoys midway between Ile de Groix and Gavres). DREV and NRaD with NAVEURMETOCCEN made upper-air observations using radiosondes.

The participants agreed to document their particular measurements and share data on a case-by-case basis. In fulfillment of this agreement, the measurement program will be reviewed briefly in this report (greater detail will be available from the other national reports). First, the physics of the surface layer meteorological models will be examined; next, surface and upper-air measurements made by NRaD and NAVEURMETOCCEN will be presented; and, finally, some calculations of expected ray angles-of-arrival will be analyzed.

Table 1. List of participants.

Country	Participant
Canada	Defense Research Establishment Valcartier (DREV)
France	Centre d'Electronique de l'Armement (CELAR) Centre d'Etudes et de Recherches de Toulouse (CERT)
Germany	Forschungsgesellschaft fuer Angewandte Naturwissenschaften—Forschungsinstitut fur Hochfrequenzphysik (FGAN—FHP)
Netherlands	Fysisch en Elektronisch Lab. TNO (FEL/TNO)
United States	Naval Command, Control and Ocean Surveillance Center, RDT&E Division (NRaD) Naval European Meteorology and Oceanography Center (NAVEURMETOCCEN)

MEASUREMENT PROGRAM

OVERVIEW

Figure 1 shows the geographical region near Lorient, France, in the Bay of Biscay. A 9.8-km overwater propagation path extends from Ile de Groix to Gavres and is shown by the dashed line. The transmitters were mounted approximately 14.8 meters above mean sea level on Ile de Groix and the receivers were mounted between 6 and 10 meters above mean sea level at a site near Gravres. Tidal variations in this area are about 2 meters. At high tide, the radio horizons are 14.7 km for the transmitter and 8.2 and 11.6 km, respectively, for the low- and high-sited receiver antennas. Even at high tide, the propagation path is well within the radio horizon. Winds blowing from the east-southeast (about 140 degrees) through due west (270 degrees) are considered to be from the sea. With winds from these directions, it is assumed that the meteorological measurements made at the receiver site (near Gavres) are representative of conditions along the propagation path. Winds blowing from northwest, through north, through east-southeast are considered continental winds. These continental winds indicate that the meteorological measurements at the receiver site are probably not representative of conditions along the propagation path.

Table 2 lists the data and time of each upper-air sounding that was made by NRaD and NAVEUR-METOCCEN. Surface meteorological observations of pressure, air temperature, relative humidity, wind speed, wind direction, and sea surface temperature are listed in this table. These observations were made typically a few minutes before the radiosonde launch. Two columns, one labeled "Surface Roughness" and the other labeled "Monin-Obukhov Length," list important parameters that are derived from considerations of the energy balance in the surface layer. These parameters are examined in the following section. The last three columns in this table list estimates of the modified refractivity gradient with respect to height. These gradients are discussed in subsequent sections.

Table 2. Dates and times of radiosondes launched. Pertinent surface layer and mixed layer meteorological parameters are also listed.

Day of Sept 1993	Time, GMT	Surface Pressure, mb	Air Temp, °C	Rel Humid, %	Wind Spd, kn	Wind Dir, deg	Sea Temp, °C	Surface Roughness, Z_0 , m	Monin-Obukhov Length, L' , m	dM/dZ from PP-11	dM/dZ from MRS	dM/dZ from LKB
15	0730	991.0	16.1	84.0	24.0	240.0	15.9	+4.552E-04	-4.447E+03	0.1254	0.1167	0.1160
15	1730	1002.0	16.3	62.0	10.0	310.0	16.6	+1.535E-04	-8.202E+01	0.1214	0.1235	0.1206
16	0715	1010.0	14.7	71.0	8.0	310.0	15.5	+1.034E-04	-3.723E+01	0.1311	*0.0873	0.1258
16	1100	1012.0	15.7	76.0	8.0	280.0	16.7	+1.035E-04	-3.381E+01	0.1255	0.1159	0.1264
16	1415	1014.0	15.9	71.0	9.0	290.0	16.7	+1.266E-04	-5.123E+01	0.1276	0.1276	0.1251
17	0715	1018.0	9.0	79.0	2.0	20.0	15.1	+3.550E-05	-3.779E-01	*0.0642	*0.1078	0.1297
17	1115	1018.0	15.8	57.0	3.0	50.0	17.5	+2.662E-05	-2.189E+00	0.1294	—	0.1292
17	1130	1018.0	15.8	57.0	3.0	50.0	17.5	+2.662E-05	-2.189E+00	0.1427	0.1402	0.1292
17	1415	1015.0	16.2	62.0	5.0	240.0	18.0	+4.188E-05	-6.168E+00	0.1207	0.1185	0.1278
20	1200	1016.0	16.6	94.0	5.0	170.0	17.0	+4.188E-05	-4.131E+01	*0.0978	*0.0976	0.1301
20	1430	1016.0	16.4	86.0	5.0	180.0	17.0	+4.188E-05	-2.074E+01	0.1161	0.1199	0.1290
21	0800	1015.0	15.9	82.0	7.0	250.0	16.4	+7.598E-05	-4.465E+01	0.1160	0.1243	0.1276
21	1130	1018.0	17.0	74.0	10.0	240.0	17.2	+1.528E-04	-1.556E+02	0.1274	0.1328	0.1236
21	1400	1018.0	17.0	73.0	9.0	250.0	17.5	+1.261E-04	-7.239E+01	0.1234	0.1202	0.1249
22	0700	1013.0	11.6	84.0	2.0	90.0	15.6	+3.638E-05	-5.667E-01	0.1187	0.1206	0.1298
22	0730	1012.0	12.3	83.0	2.5	105.0	15.7	+3.043E-05	-1.003E+00	0.1285	0.1117	0.1297
22	1100	1016.0	15.5	65.0	6.0	235.0	17.0	+5.727E-05	-1.100E+01	0.1420	0.1193	0.1273
22	1400	1015.5	16.8	60.0	5.0	240.0	18.0	+4.188E-05	-8.030E+00	0.1171	*0.1083	0.1275
23	1130	1017.0	18.5	56.0	3.0	60.0	16.8	+3.208E-05	+4.676E+00	0.1272	0.1194	-2.7968
23	1400	1016.5	16.8	73.0	8.0	300.0	18.0	+1.038E-04	-2.863E+01	0.1144	0.1166	0.1262

NAVEURMETOCEN provided a two-man Mobile Environmental Team (MET) with equipment and sensors to make both surface and upper-air meteorological measurements. The upper-air equipment consisted of a standard US Navy Mini Rawin System (MRS) and Vaisala RS-80 radiosondes with a wind velocity and direction capability. The MRS is a sophisticated receiver and processing system. It receives RF signals, at 403 MHz, transmitted by the radiosonde as a helium-filled balloon carries the radiosonde through the atmosphere. The radiosonde instrument package directly senses the pressure, temperature, and relative humidity of the air parcel and telemeters this information back to the ground-based MRS receiver as raw data (a pulse-width modulated signal). In addition, it retransmits a NAVAID signal (typically OMEGA) back to the MRS, which processes this retransmitted data to determine wind direction and speed. Internally, the MRS monitors the raw pressure, temperature, and humidity data stream (a new value is sent about once every 1.5 seconds), converts the raw data into true units (mb, °C, and percent). It also computes the height and refractivity. Further, the processor smooths the data, removes outliers, and provides a number of display and output options.

NRaD upper-air equipment consisted of a Vaisala model PP-11 processing system, which is less sophisticated than the MRS. The PP-11 receives and decodes the same raw pressure, temperature, and humidity data stream as the MRS, but the PP-11 simply converts the data (to true units of mb, °C, and percent) and outputs the converted stream as a set of ASCII characters. There is no smoothing or any additional processing of the data.

Both the MRS and the PP-11 read a punched-paper tape to get a set of coefficients that are used to convert the raw data stream into true units. Each radiosonde is calibrated at the factory and has its own punched tape. However, the PP-11 and MRS conversion algorithms are identical.

Although less than half the observations may be considered representative of conditions along the propagation path, there is one case where, for two days in a row, the winds were from the sea. Therefore, the analysis will concentrate on measurements made on these two days—20 and 21 September. However, before proceeding into the data analysis, the meteorological models will be quickly reviewed (greater details are readily available in the open-literature citations).

METEOROLOGICAL MODEL OF THE SURFACE LAYER

Radio wave propagation in the troposphere is controlled by the spatial distribution of the radio refractive index, n , and by the surface characteristics. A numerically convenient term is the refractivity N that is related to the refractive index by $N = (n - 1)10^6$. The refractivity of a parcel of air is

$$N = \frac{77.6}{T} \cdot \left(P + \frac{4810 \cdot E}{T} \right) \quad (1)$$

where T is the temperature in Kelvin, P is the pressure in mb, and E is the water vapor pressure in mb. For a standard or normal atmosphere, the refractivity monotonically decreases with increasing height at a rate of 39 N/km [Bean and Dutton, 1966]. By Snell's Law, a ray (direction of a normal to the wave front) initially launched at an angle parallel to the earth's surface will be refracted downward as it travels in range. The curvature of the ray path is less than the curvature of the earth, so, as the ray travels in range, the height of the ray above the surface increases.

The modified refractive index, M , is a mapping of the vertical refractivity from a curved geometry to Cartesian coordinates and greatly reduces the computational complexity of radio propagation

analysis. It is defined as $M = N + (Z/a)10^6$, where Z is the height above the earth's surface and a is the earth's radius (6371 km).

In the troposphere, measurements of T , P , and RH are sufficient to compute the refractivity of the air parcel. However, close to the surface, the meteorological measurements are strongly influenced by turbulence. Instead of using the instantaneous measurements of T , P , and RH to characterize the refractivity close to the surface (in the surface layer), the accepted approach is to model the turbulent transport mechanisms and infer the refractivity.

While there is no exact definition of surface layer, qualitatively, it is that part of the atmosphere immediately above the surface where the fluxes of momentum, heat, and moisture can be considered as constant (see Panofsky and Dutton, 1983). In this layer, both mechanical and thermal forcing affect the turbulence and the variation of the mean wind speed, temperature, and humidity. Monin and Obukhov [1954] introduced two scaling parameters for velocity and length that are independent of height in the surface layer. The parameters are the friction velocity, U_* , and a length L that depends only on the fluxes of heat and moisture and the friction velocity.

In the surface layer, the vertical gradient of a conservative property i is related to its vertical flux S_i by

$$\frac{\partial i}{\partial z} = \frac{S_i}{\rho \cdot k \cdot U_* (Z + Z_0)} \Phi \quad (2)$$

where ρ is the atmospheric density, k is von Karmen's constant (0.4), U_* is the friction velocity, Z_0 is a surface roughness parameter, and Φ is a stability function. Jeske [1973] proposed that Φ take the form of the Monin–Obukhov logarithmic-linear model

$$\Phi = 1 + \alpha \frac{Z}{L'} \quad (3)$$

for stable conditions (air warmer than the sea) and that Φ take the form of the *KEYPS* relation [Lumley and Panofsky, 1964]

$$\Phi^4 - 4\beta \frac{Z}{L'} \Phi^3 = 1 \quad (4)$$

for unstable conditions (air cooler than the sea). In these expressions, α is taken to be 5.2, β is taken to be 4.5, Z_0 is 0.00015 meter, and L' is the gradient form of the Monin–Obukhov scaling length corrected for stability. Jeske uses an empirical profile coefficient Γ to relate L' to physical observables of temperature and wind speed:

$$L' = \frac{T_a U^2 \Gamma}{g(T_a - T_s)} \quad (5)$$

where T_a is the air temperature in Kelvin, T_s is the sea surface temperature in Kelvin, g is the acceleration of gravity (9.8 m/s²), and U is the wind speed in m/s. Taking the conservative property as potential refractivity N_* , the scaling function is

$$N_* = \frac{k \cdot \Delta N_p}{\ln\left(\frac{Z_1 + Z_0}{Z_0}\right) - \psi} \quad (6)$$

where ΔN_p is the potential refractivity difference between the surface and a reference height, Z_1 , in meters. The universal stability function ψ is related to Φ through

$$\psi = \int_0^{Z/L} \left[1 - \Phi(\zeta) \frac{d\zeta}{\zeta} \right] \quad (7)$$

The vertical modified refractivity profile is computed as

$$M = 0.125 \cdot Z + \frac{N_*}{k \cdot \left[\ln\left(\frac{Z+Z_0}{Z_0}\right) - \psi \right]} \quad (8)$$

The surface layer model of Liu, Katsaros, and Businger [1979], also referred to as the LKB model, is based on simultaneously solving the diabatic profile equations for velocity, temperature, and humidity, given by

$$\frac{\Theta - \Theta_s}{\Theta_*} = \frac{\ln(Z/Z_T) - \psi_\Theta}{1.14 \cdot k} \quad (9a)$$

$$\frac{Q - Q_s}{Q_*} = \frac{\ln(Z/Z_Q) - \psi_Q}{1.14 \cdot k} \quad (9b)$$

$$\frac{U - U_s}{U_*} = \frac{\ln(Z/Z_0) - \psi_U}{k} \quad (9c)$$

where Θ is the potential temperature and Q is the specific humidity.

For unstable conditions, the stability functions are

$$\psi_\Theta = \psi_Q = 2 \cdot \ln \frac{1 + (1 - 16Z/L)^{1/2}}{2} \quad (10a)$$

$$\psi_U = 2 \cdot \ln \frac{1 + (1 - 16Z/L)^{1/4}}{2} + \ln \frac{1 + (1 - 16Z/L)^{1/2}}{2} - 2 \cdot \tan^{-1}(1 - 16Z/L)^{1/4} + \frac{\pi}{2} \quad (10b)$$

For stable conditions, the stability functions are

$$\psi_\Theta = \psi_Q = \psi_U = -7 \cdot Z/L \quad (10c)$$

The Monin–Obukhov length is

$$L = \frac{(\Theta \cdot (1 + 0.61 \cdot Q) \cdot U)^2}{g \cdot k \cdot (\Theta_* \cdot (1 + 0.61 \cdot Q) + 0.61 \cdot \Theta \cdot Q_*)} \quad (11)$$

The surface roughness parameter Z_0 is related to the wind drag coefficient C_D by

$$Z_0 = 10 \cdot \exp^{-1} \left[\frac{k}{\sqrt{C_D}} \right] \quad (12)$$

where C_D is computed for the wind speed at 10 meters, which is given by

$$U_{10} = \frac{U_* \cdot \ln\left(\frac{10}{Z_0}\right)}{k} \quad (13)$$

The remaining unknowns, Z_T and Z_Q , are related to the Reynolds roughness number, which is related to the surface roughness parameter and the friction velocity [Liu, Katsaros, and Businger, *op. cit.*].

Equations 9 through 13 are solved iteratively to obtain the estimates of the temperature, humidity, and velocity scaling functions. Equation 9 is used to calculate the vertical temperature and humidity profiles and, with the hydrostatic approximation to allow the calculation of the pressure profile, equation 1 is used to compute the vertical profile of refractivity.

The LKB model is in a sense more pleasing than the Jeske formulation in that it does not require an empirical connection between L' and the physical observables. The added complexities of solving three equations for three unknowns are generally insignificant except in highly stable conditions where the problem is ill-formed and the iterations fail. There are probably techniques for solving these ill-formed problems, but that topic is beyond the scope of this analysis.

RESULTS

METEOROLOGICAL MEASUREMENTS

The values of Z_0 and L' , derived from the LKB formalism, are listed in table 2. Figures 2 through 21 show the vertical modified refractivity profiles corresponding to the entries in table 2. Data processed by the PP-11 are shown as open circles; data processed by the MRS are shown as crosses. The solid line is the M profile, calculated using the LKB formalism, for the surface observations listed in table 2. Estimates of the modified refractivity vertical gradient (dM/dZ) are listed in the last three columns of table 2. Gradients derived from radiosonde measurements are calculated by fitting a linear regression line to the PP-11 and MRS observations in the height interval of 100 to 250 meters. The gradients derived from the bulk measurements are calculated by fitting a linear regression line to the LKB M profile in the height interval of 50 to 100 meters. Figure 22 compares these M gradients showing dM/dZ calculated using LKB techniques as the abscissa and dM/dZ derived from the radiosondes as the ordinate. There is generally good agreement between the gradients derived from upper-air observations and the gradients computed from bulk surface measurements. There are six cases that are not plotted in figure 22. These cases are marked with an asterisk in the dM/dZ columns of table 2. On the days of 16 and 17 September, the significant discrepancies in the gradients are likely attributable to errors in processing by the PP-11 and MRS. Figures 4 (MRS failure) and 7 (MRS and PP-11 failure) clearly illustrate these errors. The discrepancies on 20 September (see figure 11) are not so easily explained, but may have resulted from inadequate surface measurements. The radiosonde measurements appear to show a surface duct about 10 meters thick, whereas the surface layer model shows a surface duct about 1 meter thick. However, in general, there is reasonable agreement between dM/dZ measured by radiosondes and dM/dZ calculated from the surface meteorological measurements.

Figures 23 through 42 compare the vertical profiles of temperature, relative humidity, and modified refractivity of the PP-11-processed radiosonde data with the vertical profiles calculated from

the bulk surface meteorological measurements. In most of these cases, there is very good agreement between the *gradients* of the vertical profiles (from the surface to a height of 75 meters). The surface and upper-air temperature profiles around 0700 GMT are markedly different on the morning of 22 September, as shown by figures 37 and 38. In the morning, the air was cool (about 11.6°C) but rapidly increased in temperature (12.3°C half an hour later); the radiosonde measurements indicate a surface inversion layer. Part of the discrepancies in the temperature gradients may be due to radiational heating and cooling of the land (wind speed was low, about 2 knots).

Figure 41 illustrates the only strongly stable surface measurements made at Gavres. The wind speed was low, about 3 knots, and coming from the land (060 degrees). It is likely that the large differences in the temperature, humidity, and *M* profiles are due to radiational heating by the land.

ANGLE-OF-ARRIVAL ESTIMATION

Figures 43 and 44 show calculated estimates of the phase-front angle-of-arrival for frequencies of 10.5 and 35 GHz. It is assumed that the transmitter is 18.6 meters above the water, that the receiver is 10 meters above the water, and that the antennas are separated by 9.8 km. The angle-of-arrival is estimated as the real part of an eigenvalue solution to the wave equation evaluated at the surface of the ocean (see Budden, 1961). In essence, the eigenvalue should be evaluated at the receiver height, but, for the low sited antennas considered here, an evaluation at the surface should be an adequate approximation. The abscissa is the propagation factor that results from a power evaluation of each eigenvalue or mode. It includes effects of the height-gain functions and is a measure of the power contained in the mode.

Three cases are shown on each of these plots. The triangles represent estimates of the angle-of-arrival when the refractive conditions are normal (over water the gradient is 0.13 M/m). A normal atmosphere is considered as a reference atmosphere in propagation analysis. The squares represent angle-of-arrival estimates for the surface-refractive environment measured at 1130 GMT on 21 September, but with an additional assumption of a perfectly smooth ocean surface. The circles represent angle-of-arrival estimates for the surface-refractive conditions at 1130 GMT on 21 September, with a rough ocean surface corresponding to a wind speed of 10 knots. There are only slight differences between rough and smooth surface conditions.

The significant aspects of figures 43 and 44 are—

1. Propagation assessments using the measured meteorological conditions imply that the angle-of-arrival changes from about 1.5 mrad (in a normal atmosphere) to about 6.2 mrad for the specific refractive conditions measured at 1130 GMT on 21 September.
2. The changes in angle-of-arrival are approximately independent of frequency, which is in general agreement for a ray optics treatment of the propagation.
3. Surface roughness has little or no impact on the angle-of-arrival.

CONCLUSIONS

Two weeks of surface and upper-air meteorological measurements were completed in Lorient, France, in support of an international effort which was coordinated by NATO/AC243/Panel 3 Research Study Groups 8 and 21. These propagation and meteorological measurements were designed to assess the effects of the lower atmosphere on the propagation of the electromagnetic phase front at frequencies from 10 to 94 GHz.

The numerical modeling of propagation from waveguide theory at 10.5 and 35 GHz in normal and ducting environments indicates that the evaporation duct can raise the angle-of-arrival from about 1.5 mrad to about 6.2 mrad. These changes in angle-of-arrival may be significant for some close-in weapon systems. In addition, the modeling indicates that surface roughness, at least on this short path, has little or no effect on angle-of-arrival.

The indications of angle-of-arrival frequency independence should be examined in greater detail. A ray optics evaluation and comparison to the waveguide solutions may lead to additional insight into the problem of propagation assessment.

REFERENCES

- Anderson, K.D. 1990. "94 GHz propagation in the evaporation duct," *IEEE Trans. Ant. and Prop.*, vol. 38, No. 5 (May).
- . 1993. "Radar Detection of Low-Altitude Targets in a Maritime Environment," Vols. 1 and 2, NCCOSC RDTE DIV TR 1630 (Nov).
- Bean, B.R., and E.J. Dutton. 1966. *Radio Meteorology*, National Bureau of Standards Monograph 92 (March 1).
- Budden, K.G. 1961. *The Wave-Guide Mode Theory of Wave Propagation*, Logos Press, London.
- Dockery, G.D. 1988. "Propagation fade characteristics in low-altitude surface ducts," The Johns Hopkins University/Applied Physics Laboratory, Technical Report, Task 3-1-19 (October 20).
- Jeske, H. 1973. "State and Limits of Prediction Methods of Radar Wave Propagation Conditions Over Sea," *Modern Topics in Microwave Propagation and Air-Sea Interaction*, A. Zanca, Ed., Reidel Pub.
- Liu, W.T., K.B. Katsaros, and J.A. Businger. 1979. "Bulk parameterization of air-sea exchanges of heat and water vapor including the molecular constraints at the interface," *Jour. of the Atmos. Sciences*, vol. 36, pp. 1722-1735 (September).
- Lumley, J.L., and H.A. Panofsky. 1964. *The Structure of Atmospheric Turbulence*, New York: Interscience Publishers.
- Miller, A.R., R.M. Brown, and E. Vegh. 1984. "New derivation for the rough surface reflection coefficient and for the distribution of sea wave elevations," *IEE Proc.*, vol. 131, no. 2, pp. 114-116 (April).
- Monin, A.S., and A.M. Obukhov. 1954. "Basic regularity in turbulent mixing in the surface layer of the atmosphere," *Trudy Geophys. Inst. ANSSSR*, No. 24, p. 163.
- Panofsky, H.A., and J.A. Dutton. 1983. *Atmospheric Turbulence*, New York: John Wiley & Sons.

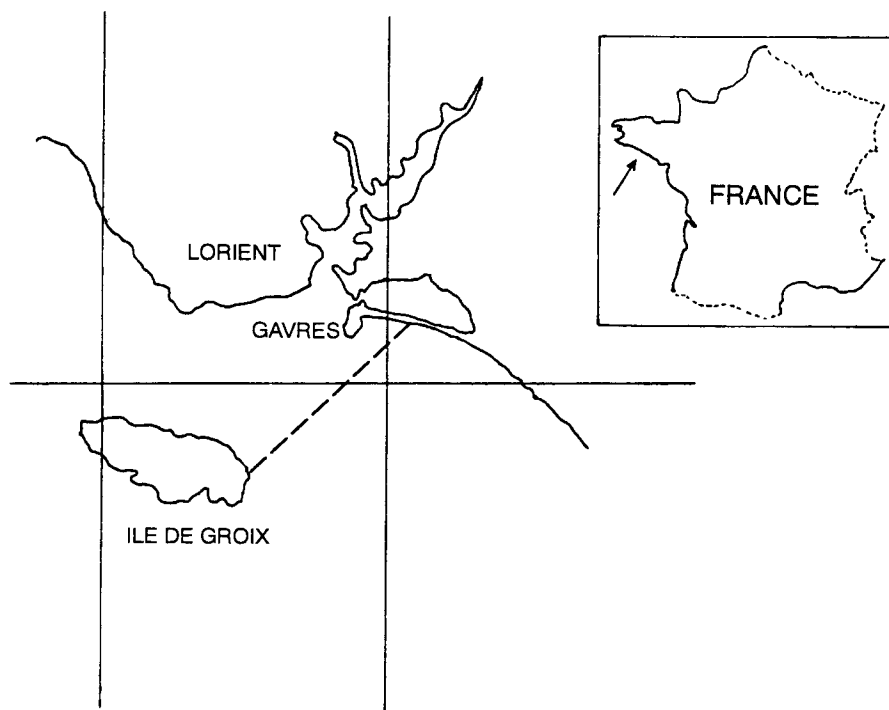


Figure 1. The geographical region around Lorient, France, in the Bay of Biscay.

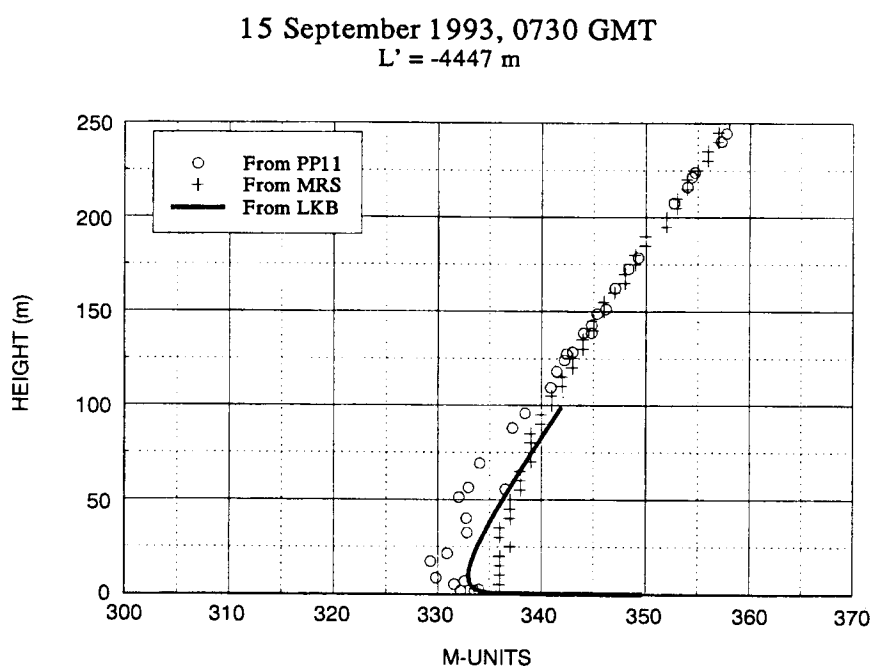


Figure 2. Vertical profiles of the modified refractivity measured by upper-air radiosondes and surface layer calculations for 15 September 1993, 0730 GMT.

15 September 1993, 1730 GMT
 $L' = -82.02 \text{ m}$

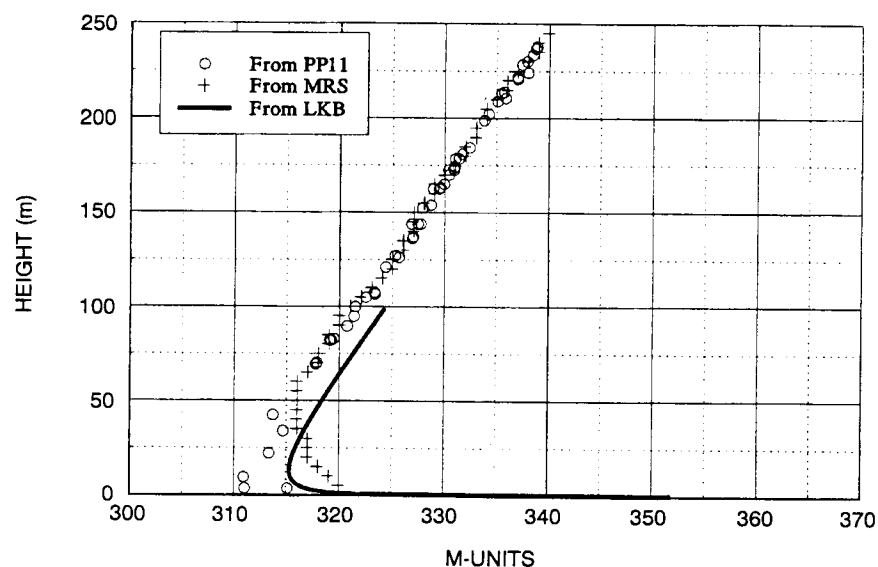


Figure 3. Vertical profiles of the modified refractivity measured by upper-air radiosondes and surface layer calculations for 15 September 1993, 1730 GMT.

16 September 1993, 0715 GMT
 $L' = -37.23 \text{ m}$

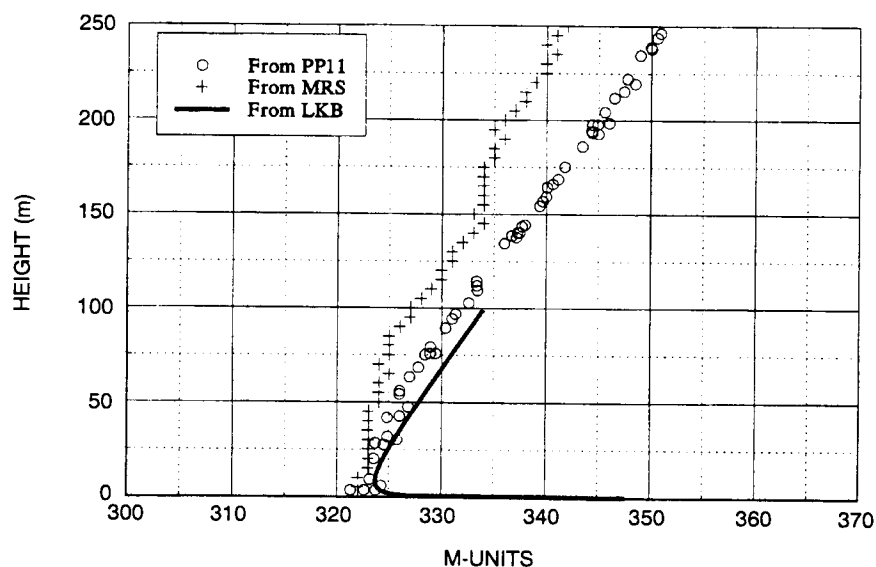


Figure 4. Vertical profiles of the modified refractivity measured by upper-air radiosondes and surface layer calculations for 16 September 1993, 0715 GMT.

16 September 1993, 1100 GMT
 $L' = -33.812 \text{ m}$

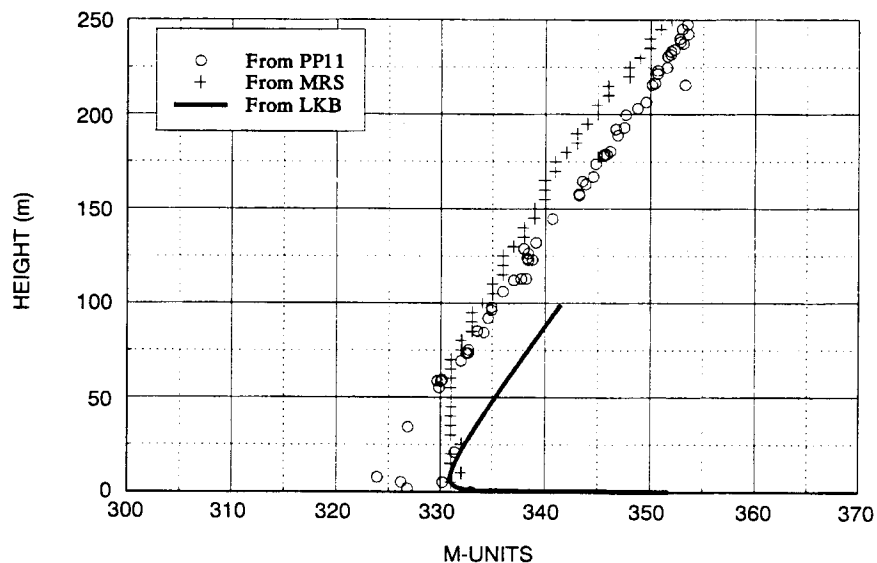


Figure 5. Vertical profiles of the modified refractivity measured by upper-air radiosondes and surface layer calculations for 16 September 1993, 1100 GMT.

16 September 1993, 1415 GMT
 $L' = -51.23 \text{ m}$

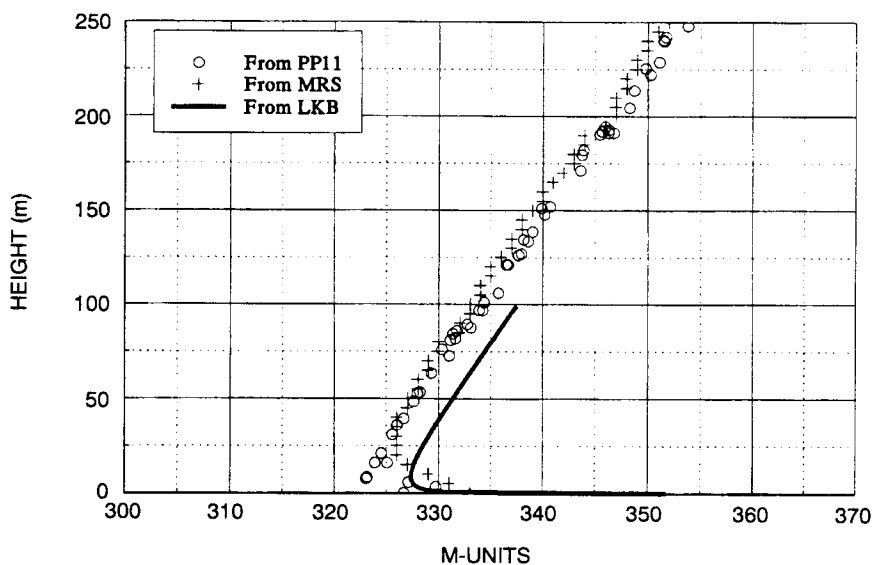


Figure 6. Vertical profiles of the modified refractivity measured by upper-air radiosondes and surface layer calculations for 16 September 1993, 1415 GMT.

17 September 1993, 0715 GMT
 $L' = -37.79$ m

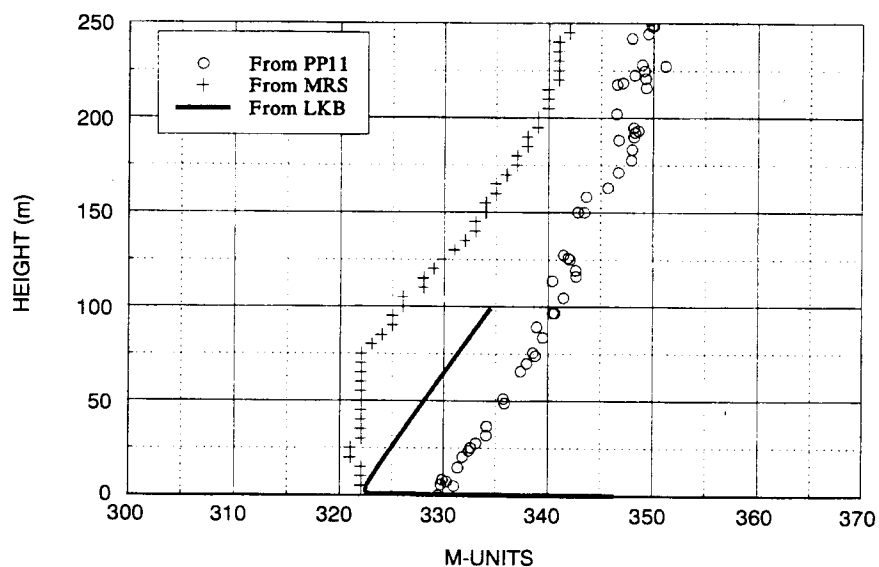


Figure 7. Vertical profiles of the modified refractivity measured by upper-air radiosondes and surface layer calculations for 17 September 1993, 0715 GMT.

17 September 1993, 1115 GMT
 $L' = -2.19$ m

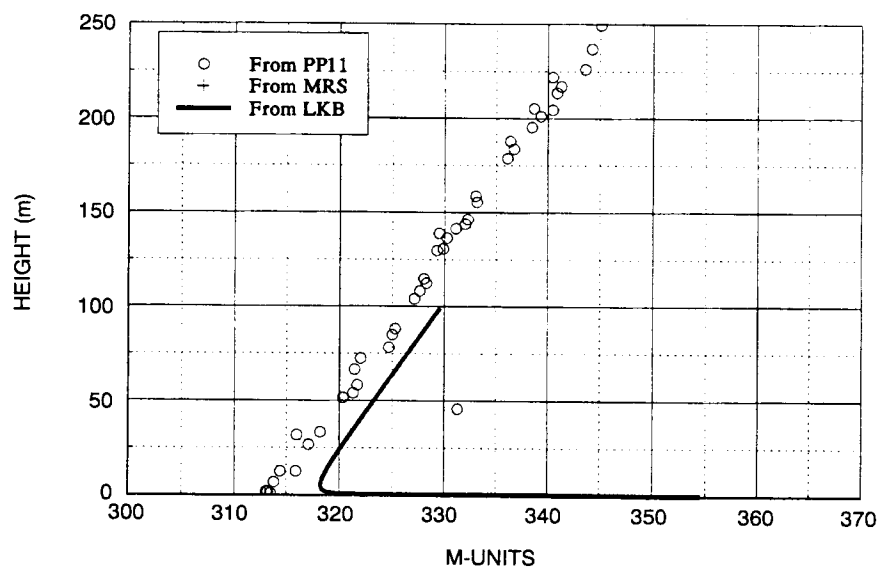


Figure 8. Vertical profiles of the modified refractivity measured by upper-air radiosondes and surface layer calculations for 17 September 1993, 1115 GMT.

17 September 1993, 1130 GMT
 $L' = -2.19$ m

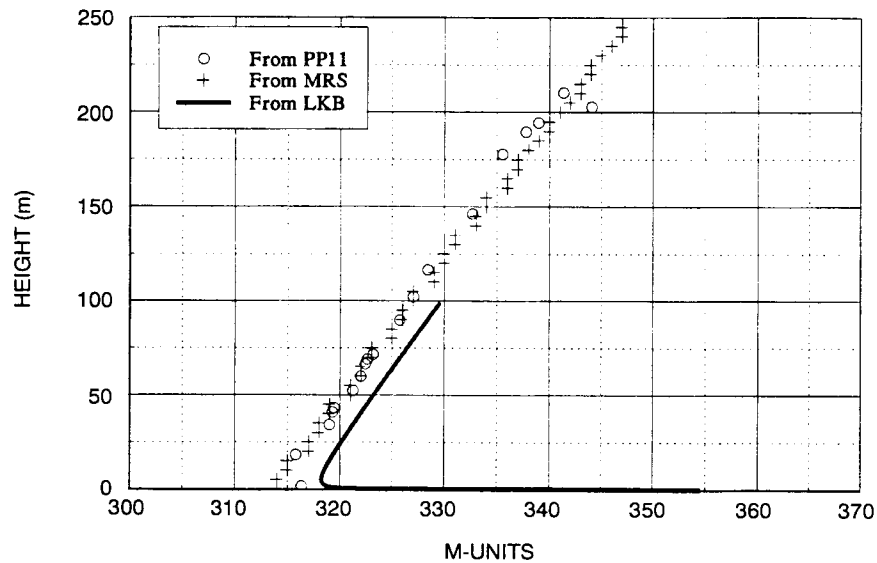


Figure 9. Vertical profiles of the modified refractivity measured by upper-air radiosondes and surface layer calculations for 17 September 1993, 1130 GMT.

17 September 1993, 1415 GMT
 $L' = -6.17$ m

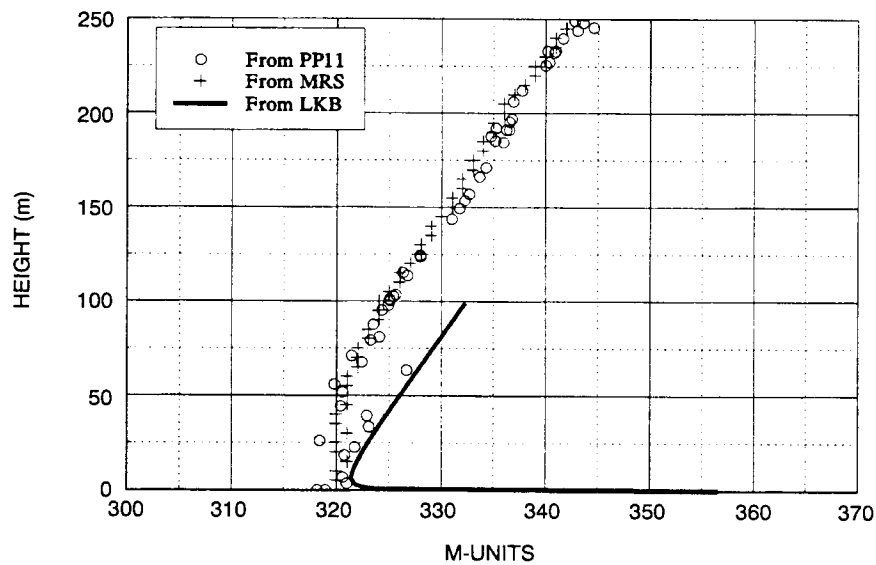


Figure 10. Vertical profiles of the modified refractivity measured by upper-air radiosondes and surface layer calculations for 17 September 1993, 1415 GMT.

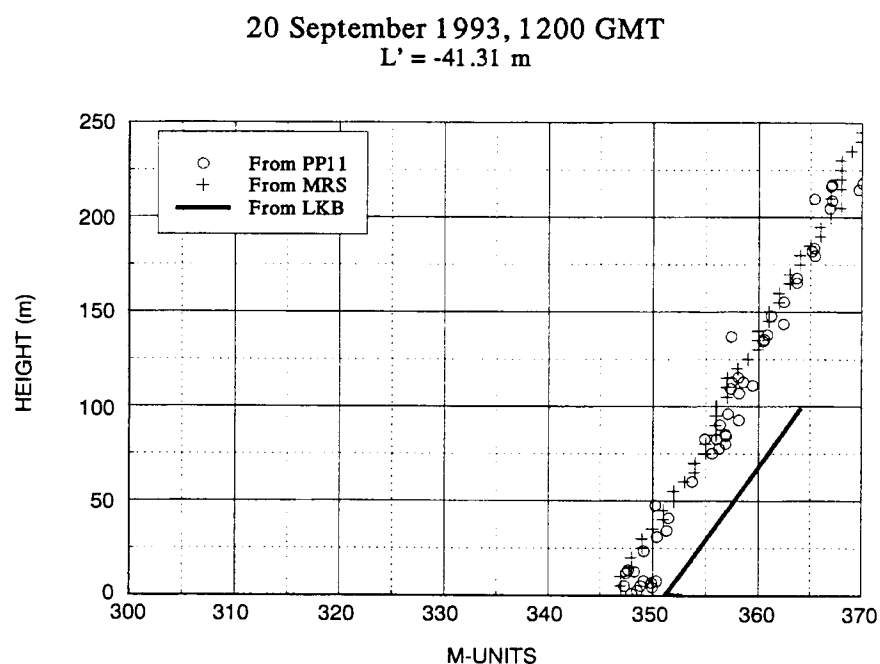


Figure 11. Vertical profiles of the modified refractivity measured by upper-air radiosondes and surface layer calculations for 20 September 1993, 1200 GMT.

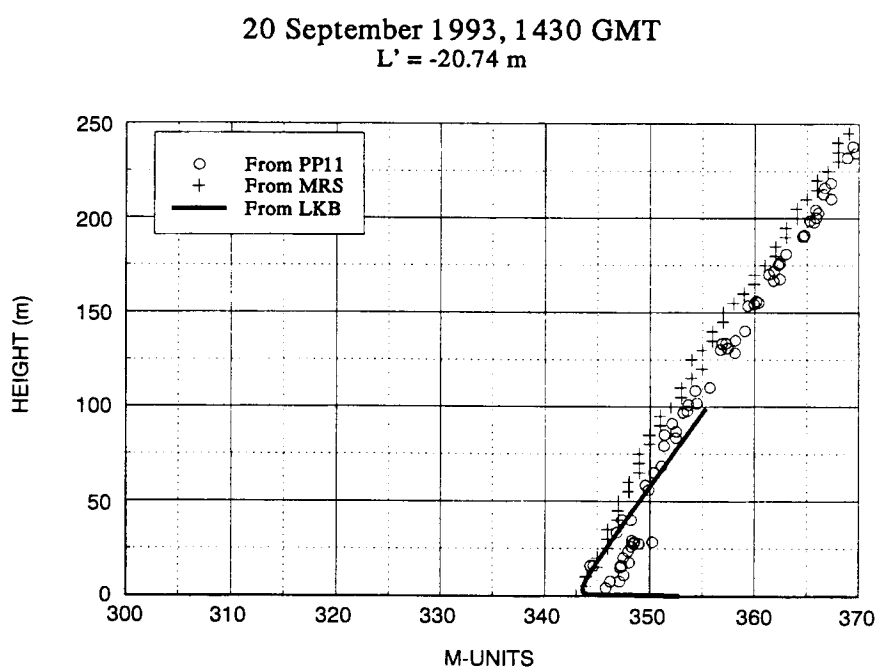


Figure 12. Vertical profiles of the modified refractivity measured by upper-air radiosondes and surface layer calculations for 20 September 1993, 1430 GMT.

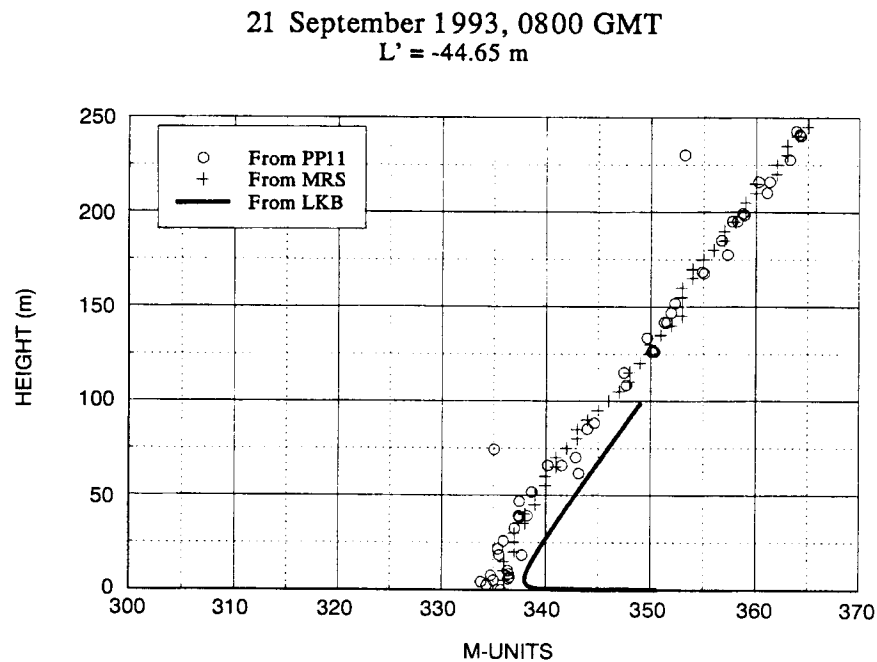


Figure 13. Vertical profiles of the modified refractivity measured by upper-air radiosondes and surface layer calculations for 21 September 1993, 0800 GMT.

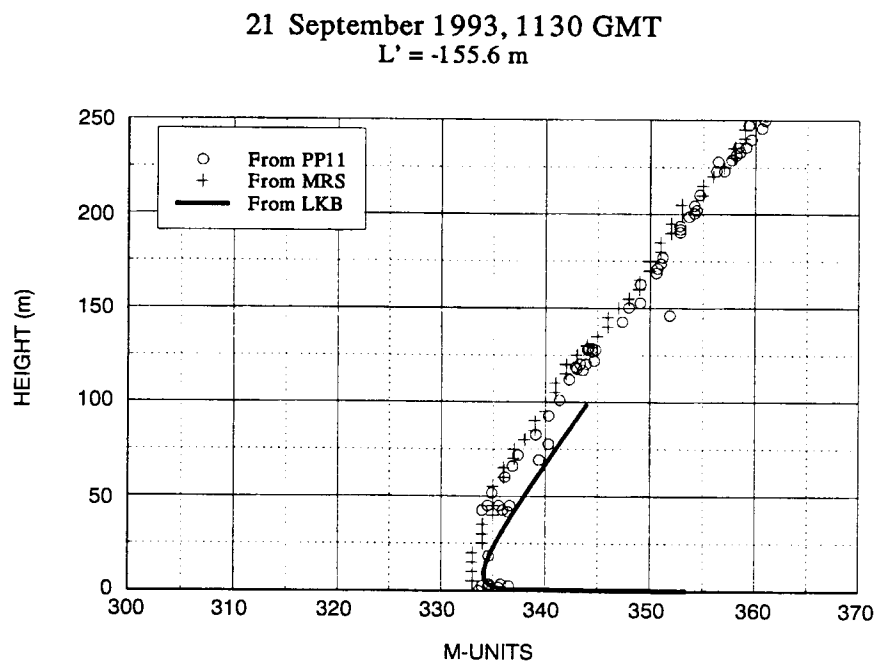


Figure 14. Vertical profiles of the modified refractivity measured by upper-air radiosondes and surface layer calculations for 21 September 1993, 1130 GMT.

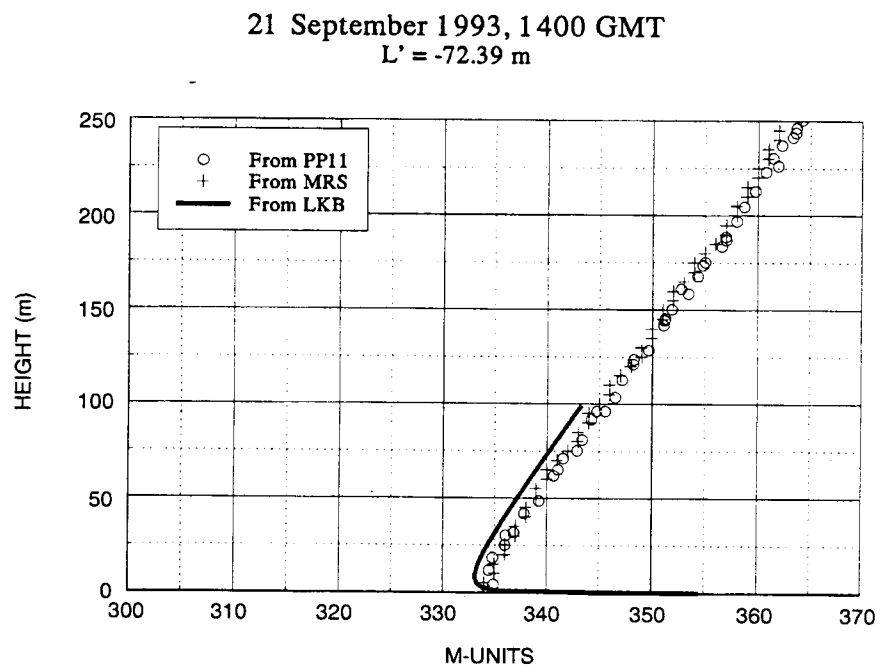


Figure 15. Vertical profiles of the modified refractivity measured by upper-air radiosondes and surface layer calculations for 21 September 1993, 1400 GMT.

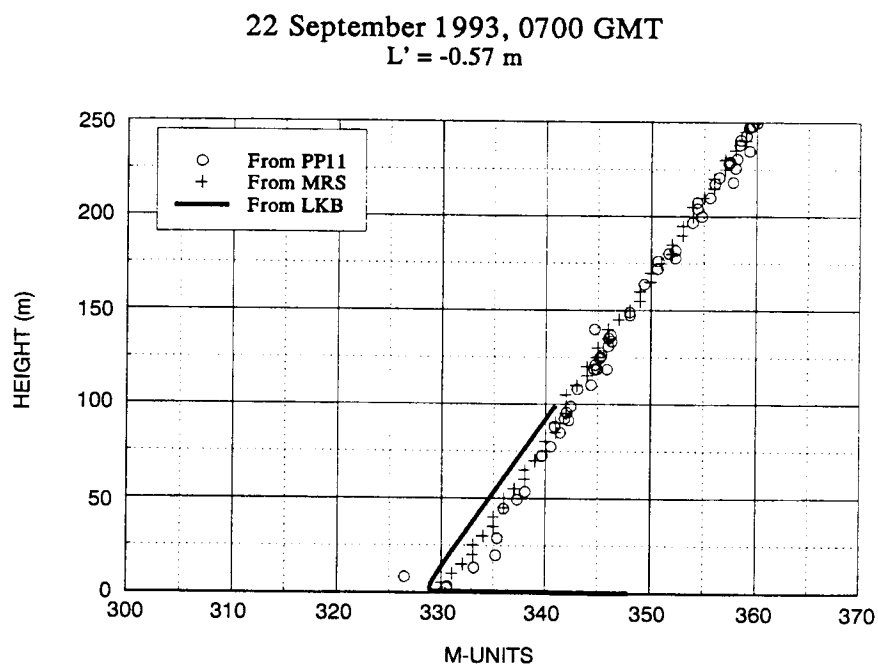


Figure 16. Vertical profiles of the modified refractivity measured by upper-air radiosondes and surface layer calculations for 22 September 1993, 0700 GMT.

22 September 1993, 0730 GMT
 $L' = -1.00$ m

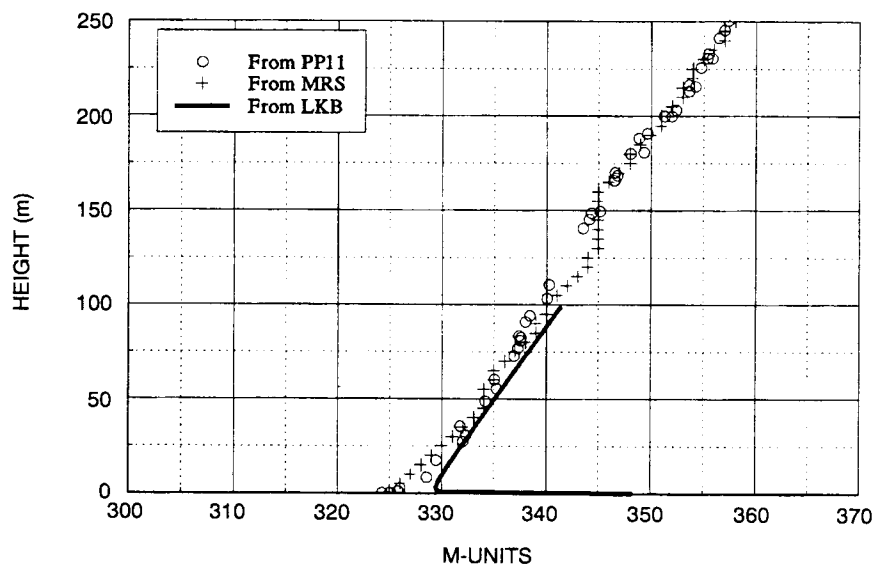


Figure 17. Vertical profiles of the modified refractivity measured by upper-air radiosondes and surface layer calculations for 22 September 1993, 0730 GMT.

22 September 1993, 1100 GMT
 $L' = -11.00$ m

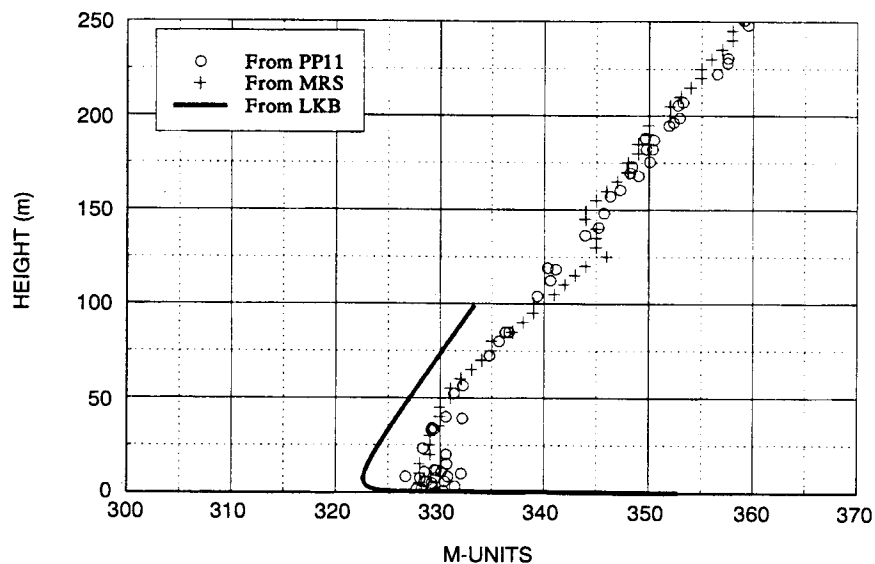


Figure 18. Vertical profiles of the modified refractivity measured by upper-air radiosondes and surface layer calculations for 22 September 1993, 1100 GMT.

22 September 1993, 1400 GMT
 $L' = -8.03$ m

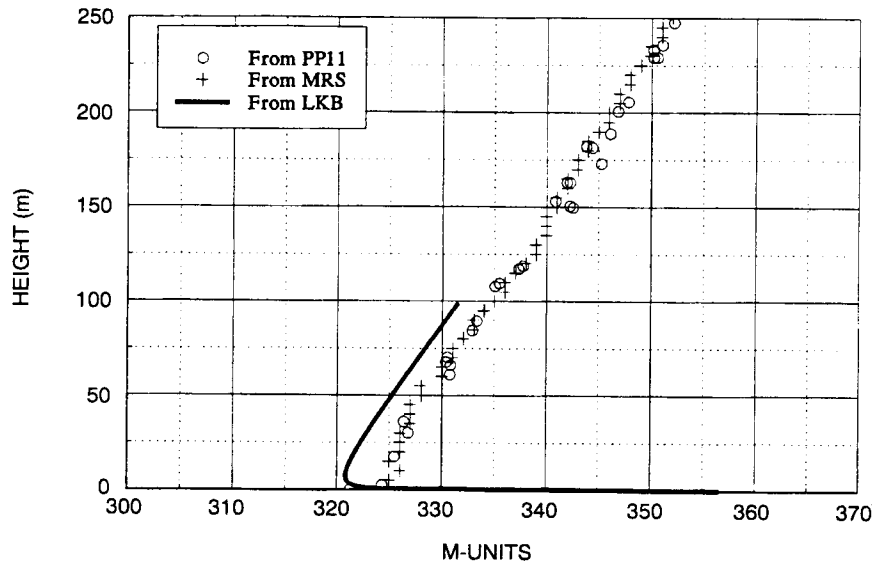


Figure 19. Vertical profiles of the modified refractivity measured by upper-air radiosondes and surface layer calculations for 22 September 1993, 1400 GMT.

23 September 1993, 1130 GMT
 $L' = +4.67$ m

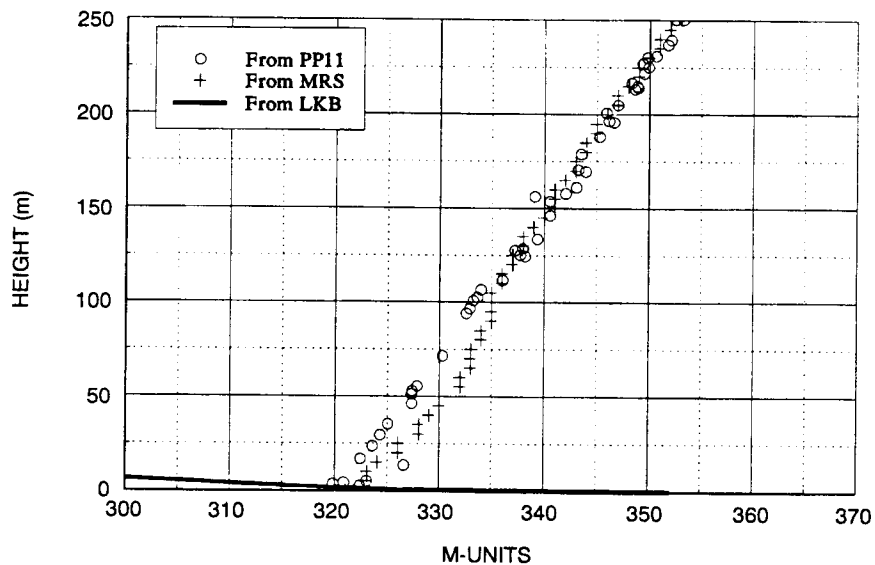


Figure 20. Vertical profiles of the modified refractivity measured by upper-air radiosondes and surface layer calculations for 23 September 1993, 1130 GMT.

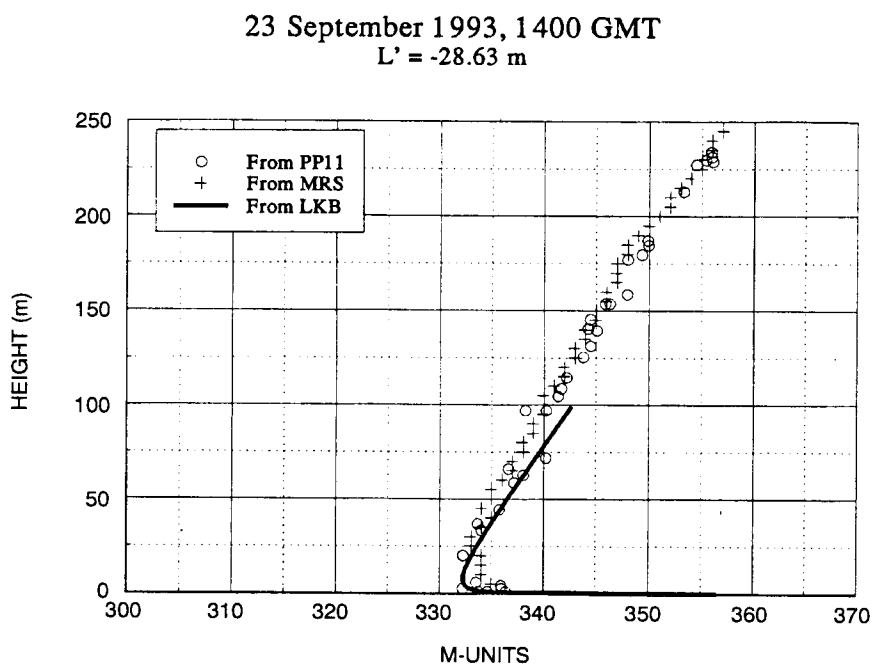


Figure 21. Vertical profiles of the modified refractivity measured by upper-air radiosondes and surface layer calculations for 23 September 1993, 1400 GMT.

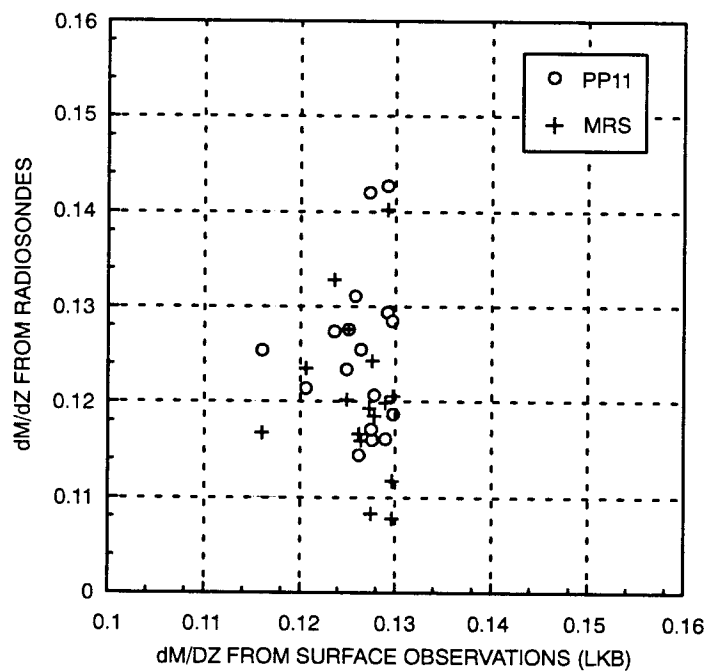


Figure 22. Gradients of modified refractivity computed from surface layer observations and compared to gradient measured by upper-air radiosondes.

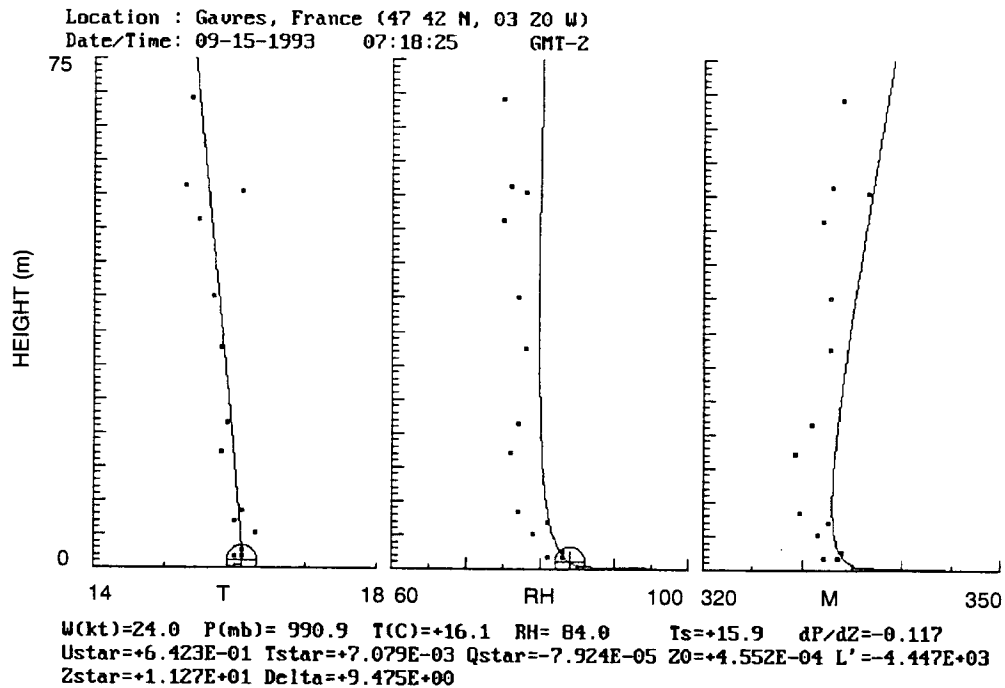


Figure 23. Vertical profiles of temperature, relative humidity, and modified refractivity measured by radiosondes (PP-11 processor) compared to profiles computed from surface layer observations for 15 September 1993, 0730 GMT.

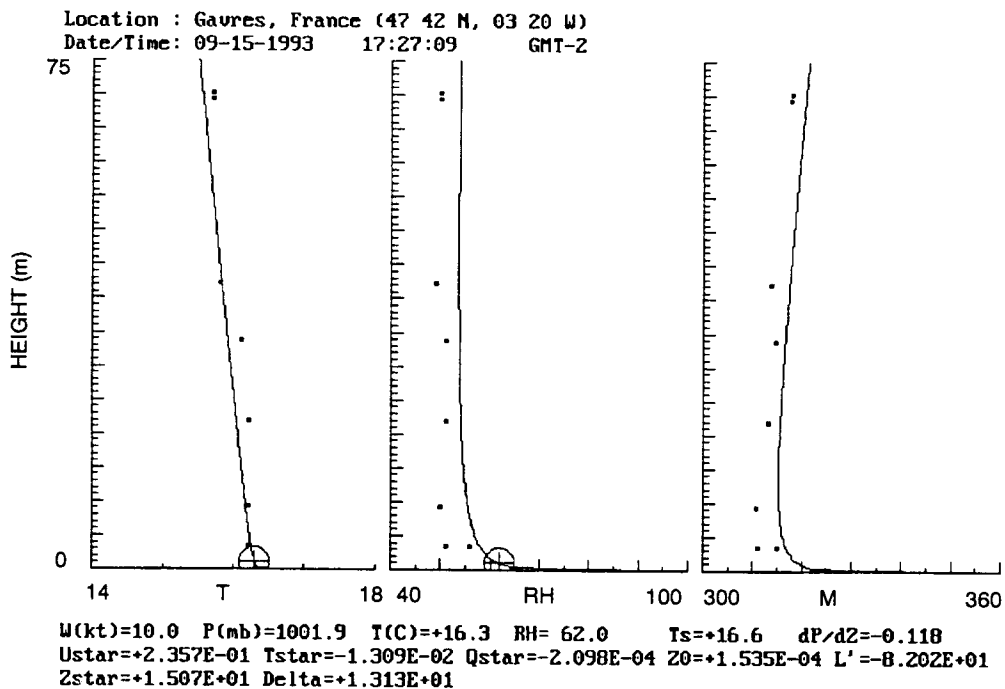


Figure 24. Vertical profiles of the modified refractivity measured by upper-air radiosondes compared to profiles computed from surface layer observations for 15 September 1993, 1730 GMT.

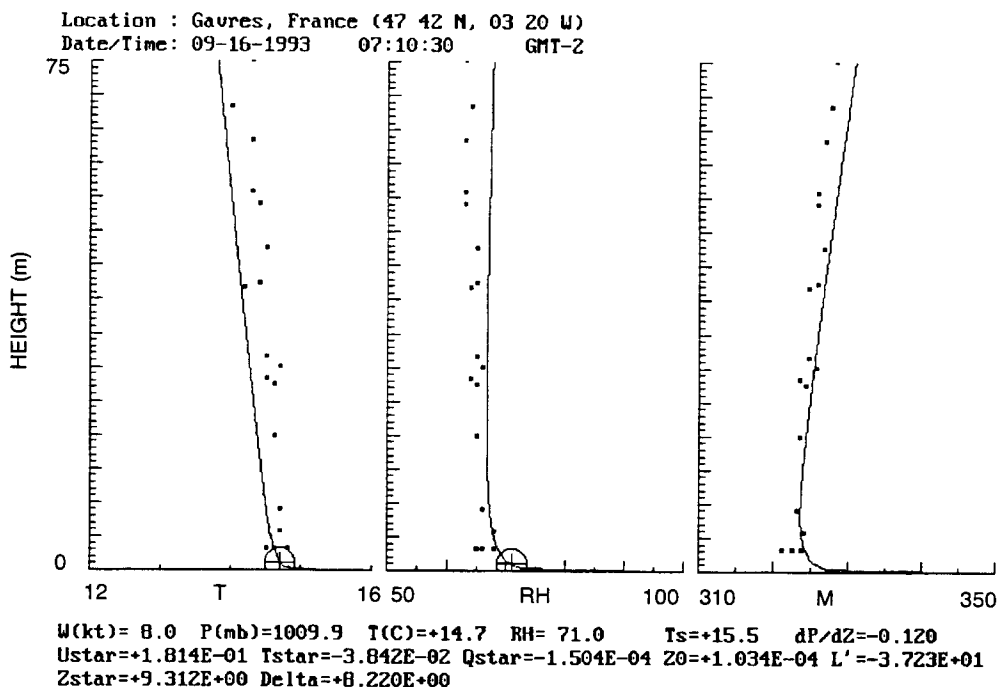


Figure 25. Vertical profiles of the modified refractivity measured by upper-air radiosondes compared to profiles computed from surface layer observations for 16 September 1993, 0715 GMT.

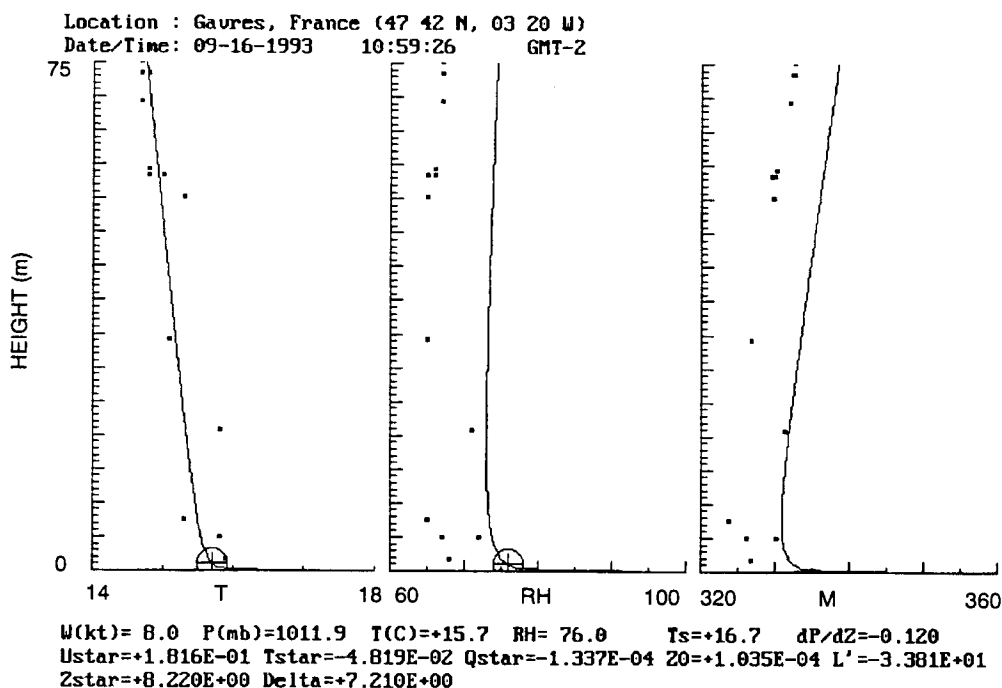


Figure 26. Vertical profiles of the modified refractivity measured by upper-air radiosondes compared to profiles computed from surface layer observations for 16 September 1993, 1100 GMT.

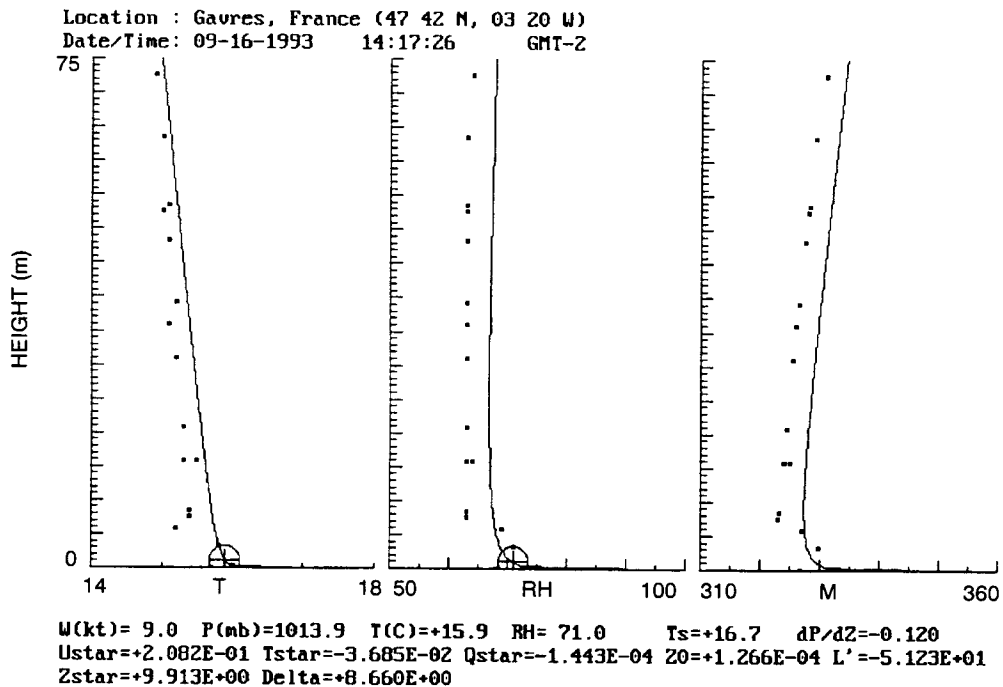


Figure 27. Vertical profiles of the modified refractivity measured by upper-air radiosondes compared to profiles computed from surface layer observations for 16 September 1993, 1415 GMT.

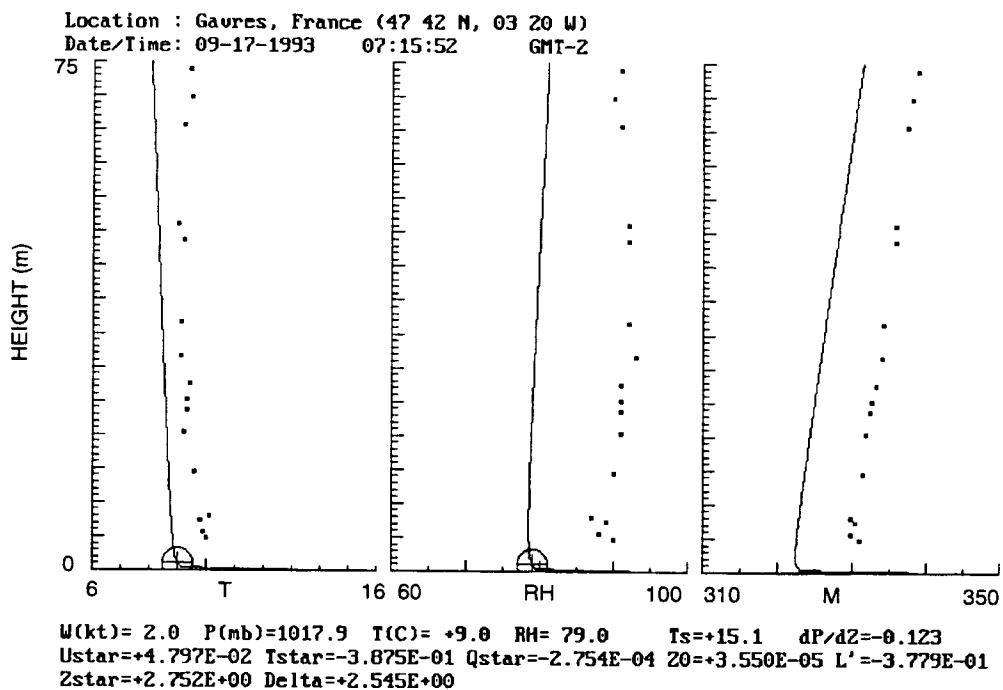


Figure 28. Vertical profiles of the modified refractivity measured by upper-air radiosondes compared to profiles computed from surface layer observations for 17 September 1993, 0715 GMT.

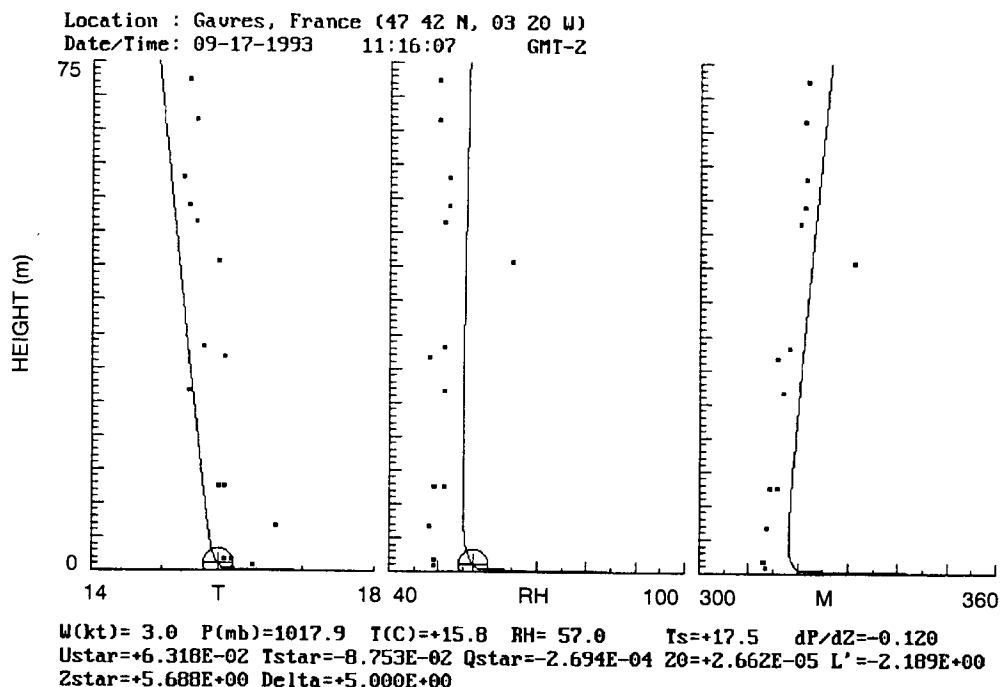


Figure 29. Vertical profiles of the modified refractivity measured by upper-air radiosondes compared to profiles computed from surface layer observations for 17 September 1993, 1115 GMT.

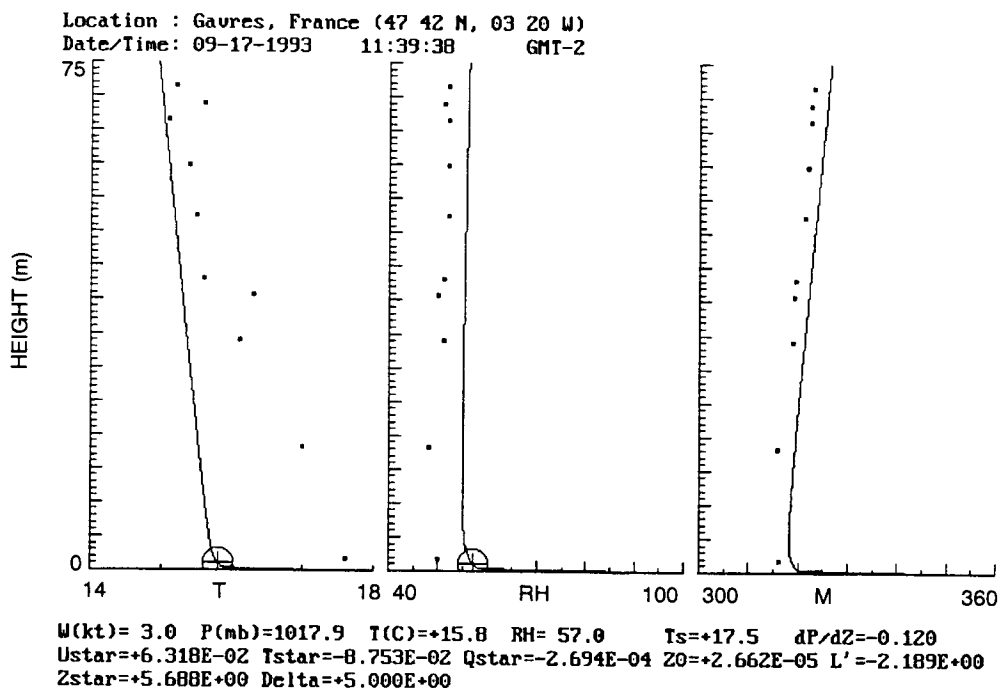


Figure 30. Vertical profiles of the modified refractivity measured by upper-air radiosondes compared to profiles computed from surface layer observations for 17 September 1993, 1130 GMT.

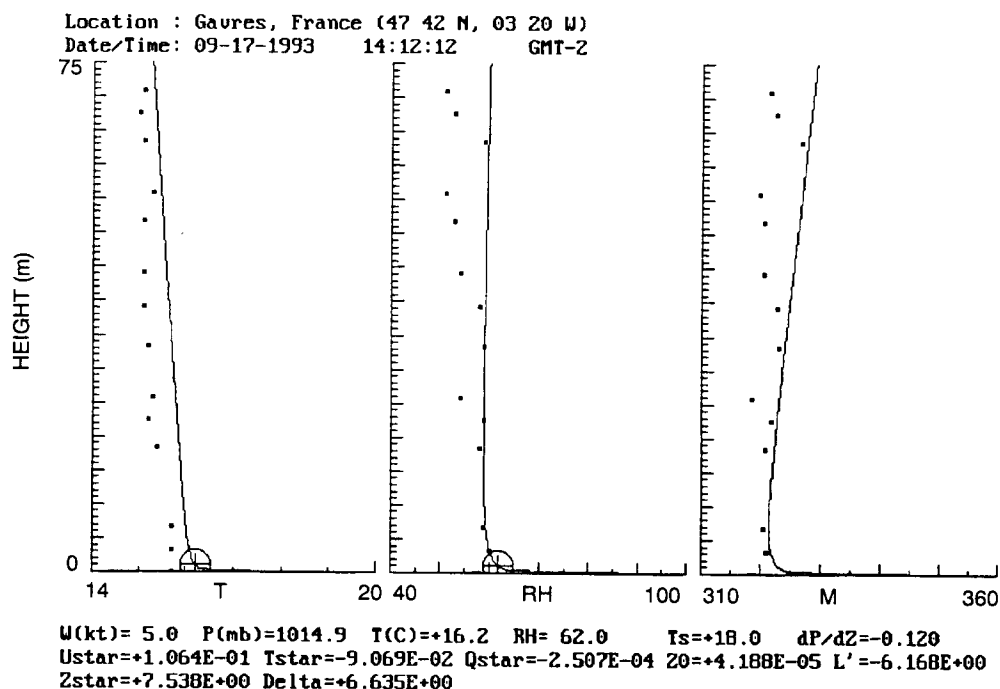


Figure 31. Vertical profiles of the modified refractivity measured by upper-air radiosondes compared to profiles computed from surface layer observations for 17 September 1993, 1415 GMT.

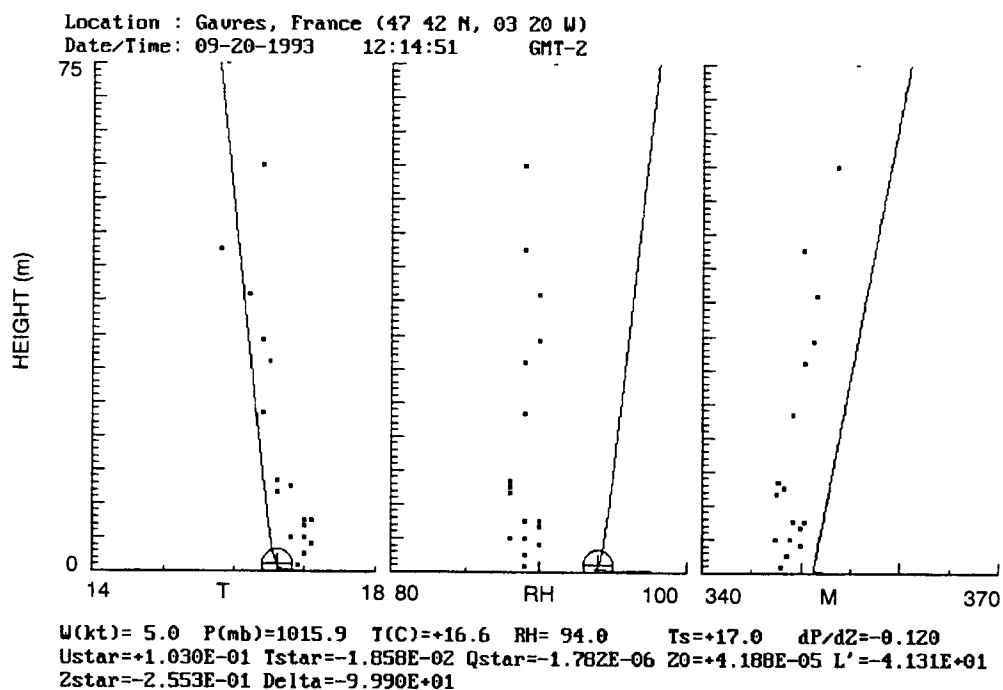


Figure 32. Vertical profiles of the modified refractivity measured by upper-air radiosondes compared to profiles computed from surface layer observations for 20 September 1993, 1200 GMT.

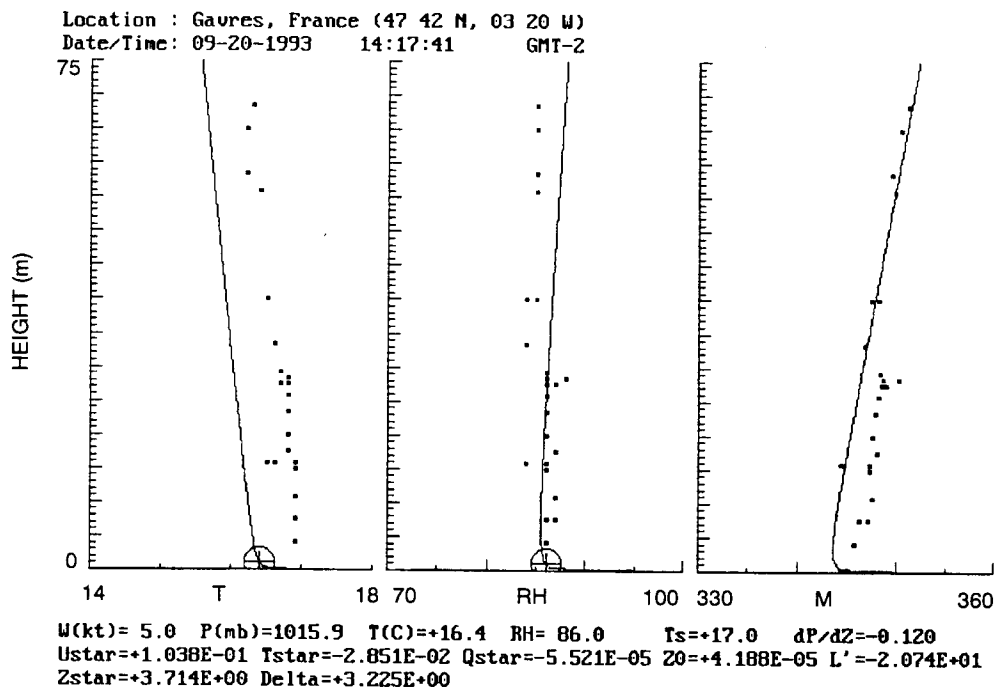


Figure 33. Vertical profiles of the modified refractivity measured by upper-air radiosondes compared to profiles computed from surface layer observations for 20 September 1993, 1430 GMT.

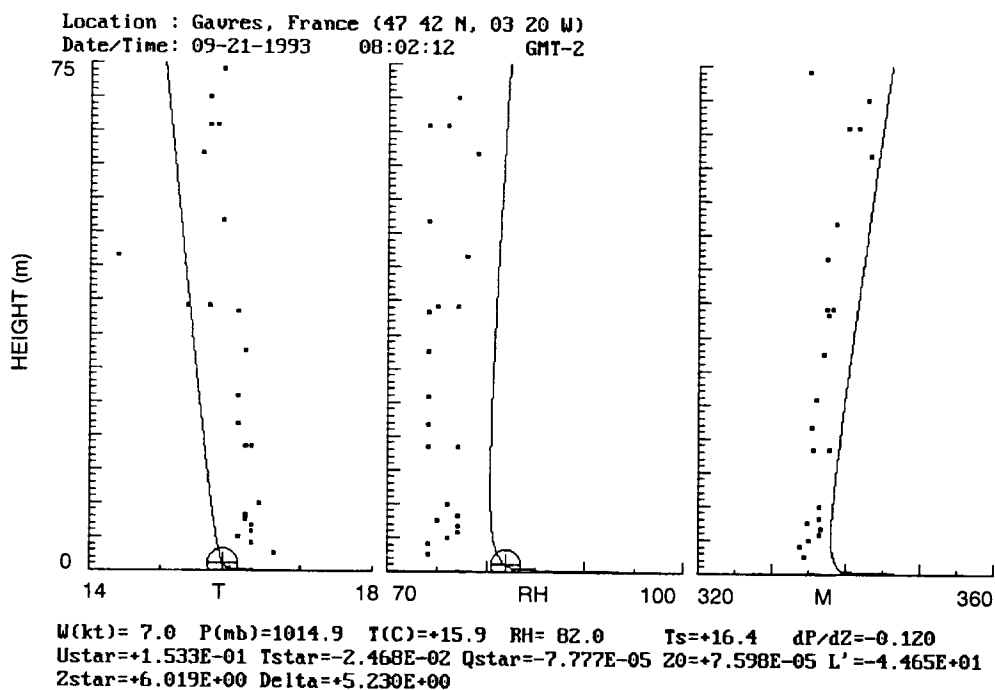


Figure 34. Vertical profiles of the modified refractivity measured by upper-air radiosondes compared to profiles computed from surface layer observations for 21 September 1993, 0800 GMT.

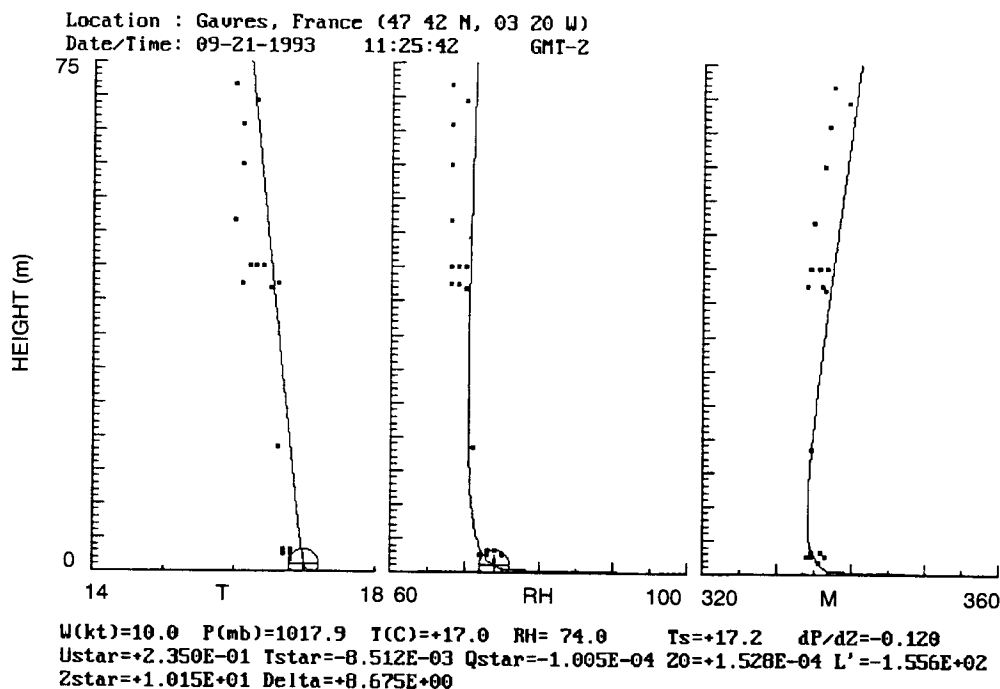


Figure 35. Vertical profiles of the modified refractivity measured by upper-air radiosondes compared to profiles computed from surface layer observations for 21 September 1993, 1130 GM.

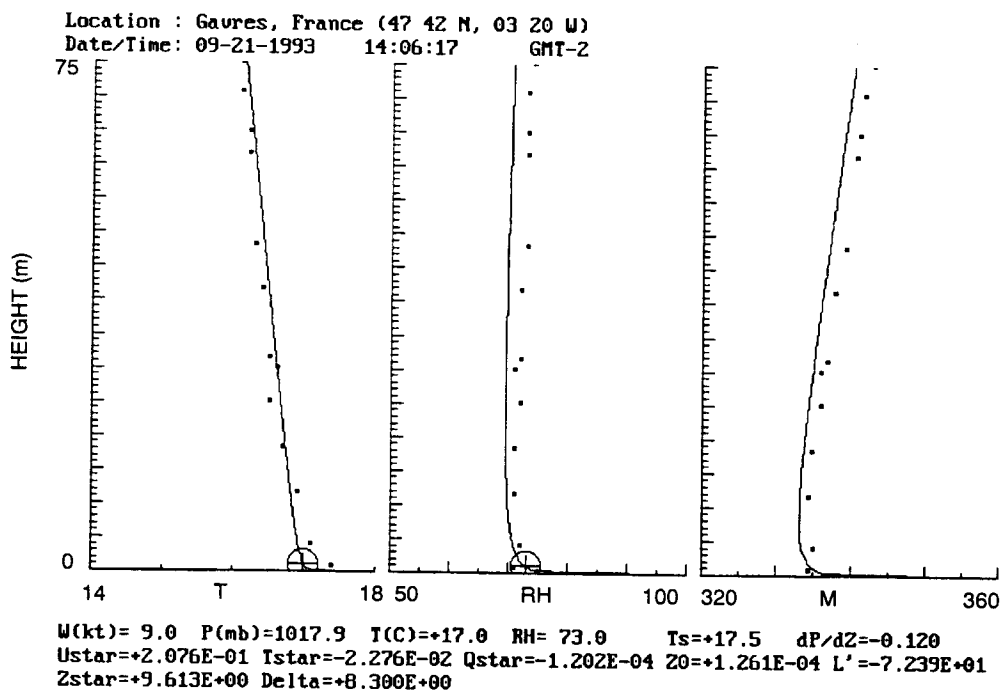


Figure 36. Vertical profiles of the modified refractivity measured by upper-air radiosondes compared to profiles computed from surface layer observations for 21 September 1993, 1400 GMT.

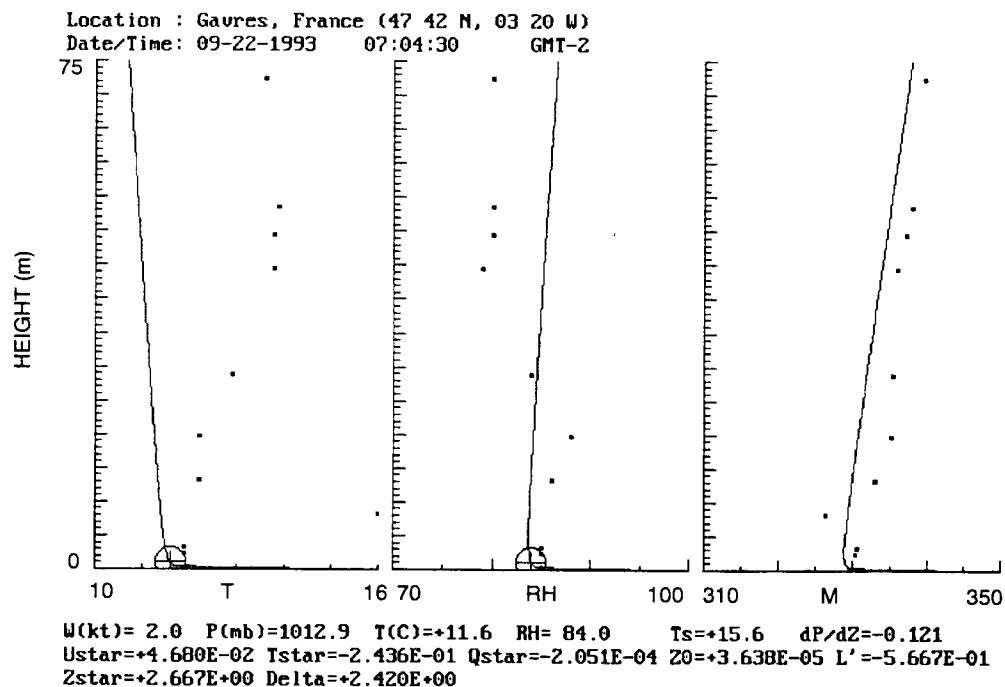


Figure 37. Vertical profiles of the modified refractivity measured by upper-air radiosondes compared to profiles computed from surface layer observations for 22 September 1993, 0700 GMT.

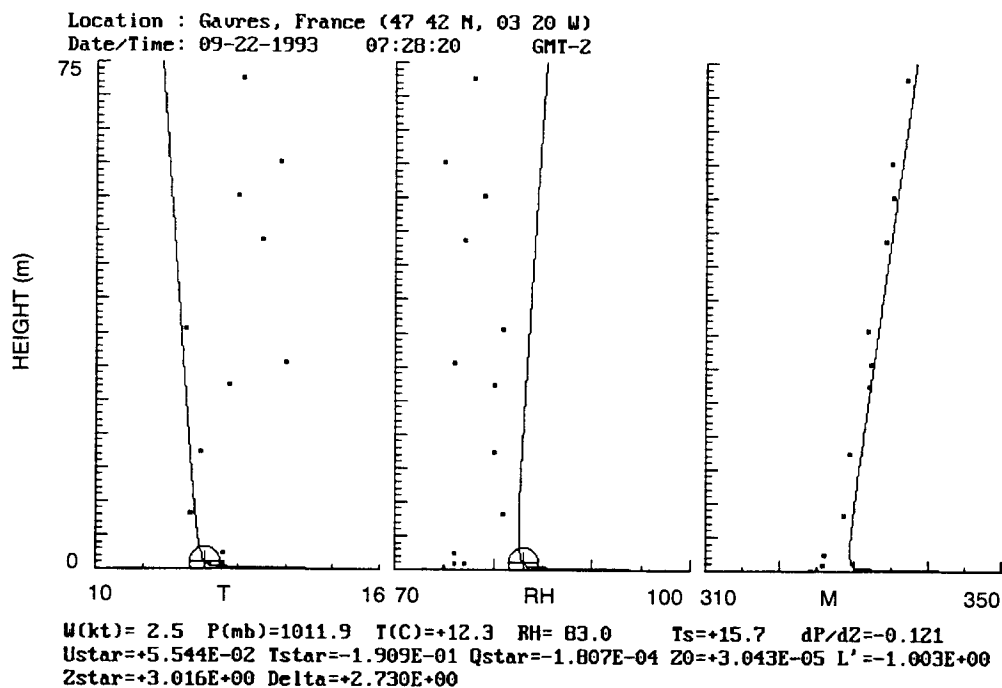


Figure 38. Vertical profiles of the modified refractivity measured by upper-air radiosondes compared to profiles computed from surface layer observations for 22 September 1993, 0730 GMT.

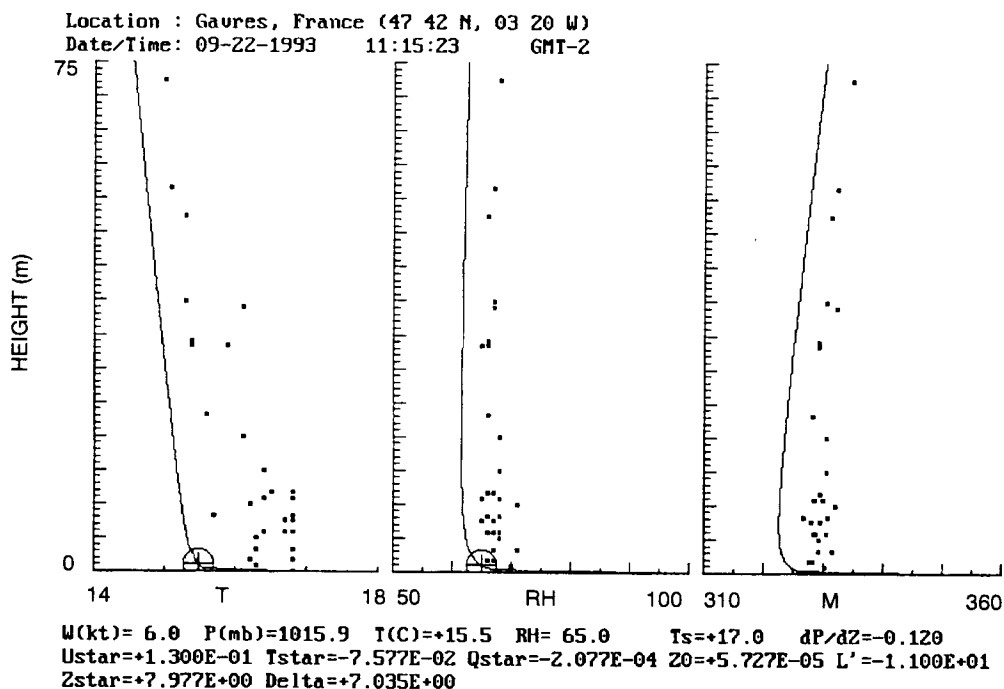


Figure 39. Vertical profiles of the modified refractivity measured by upper-air radiosondes compared to profiles computed from surface layer observations for 22 September 1993, 1100 GMT.

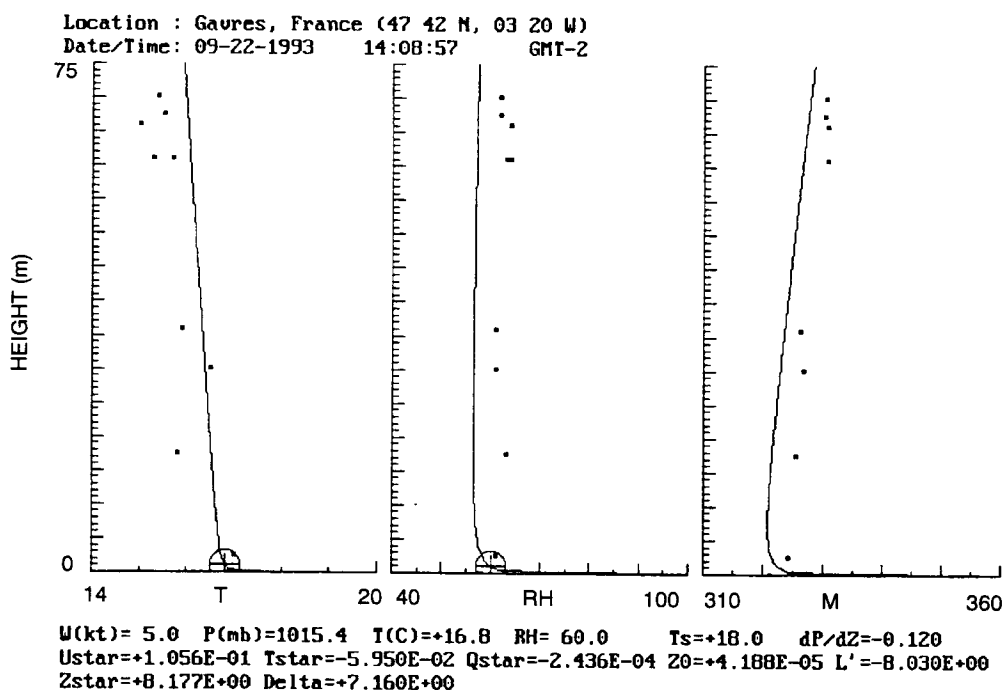


Figure 40. Vertical profiles of the modified refractivity measured by upper-air radiosondes compared to profiles computed from surface layer observations for 22 September 1993, 1400 GMT.

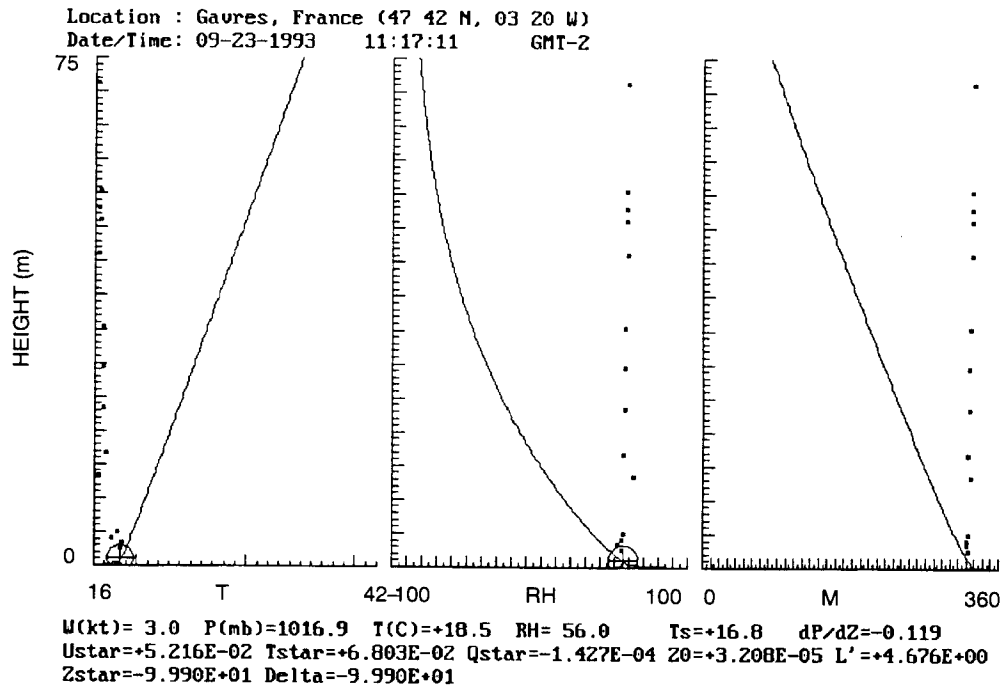


Figure 41. Vertical profiles of the modified refractivity measured by upper-air radiosondes compared to profiles computed from surface layer observations for 23 September 1993, 1130 GMT.

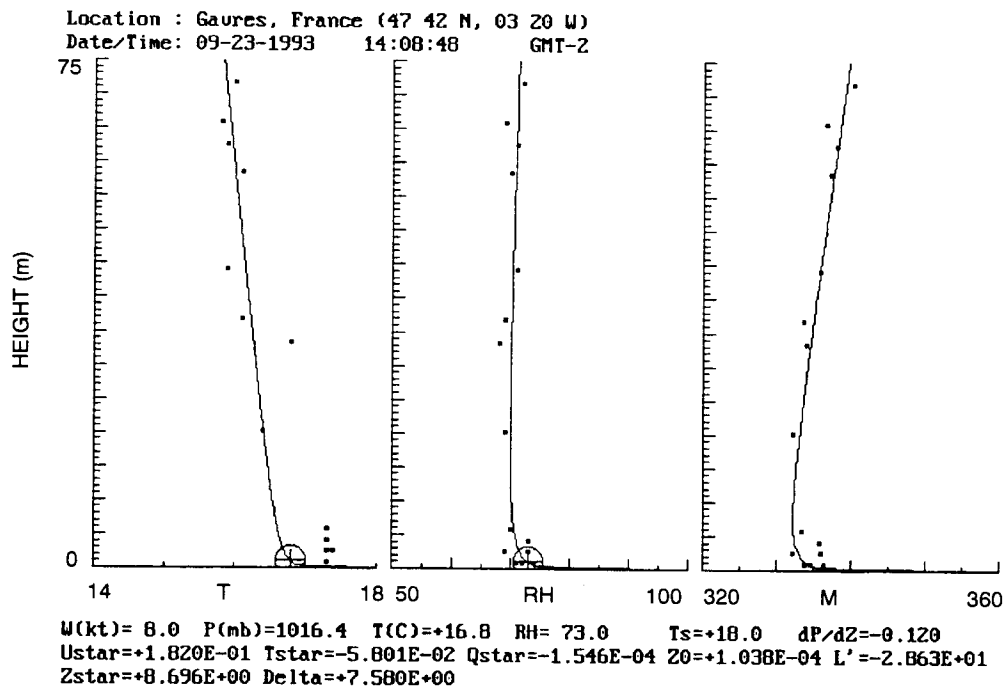


Figure 42. Vertical profiles of the modified refractivity measured by upper-air radiosondes compared to profiles computed from surface layer observations for 23 September 1993, 1400 GMT.

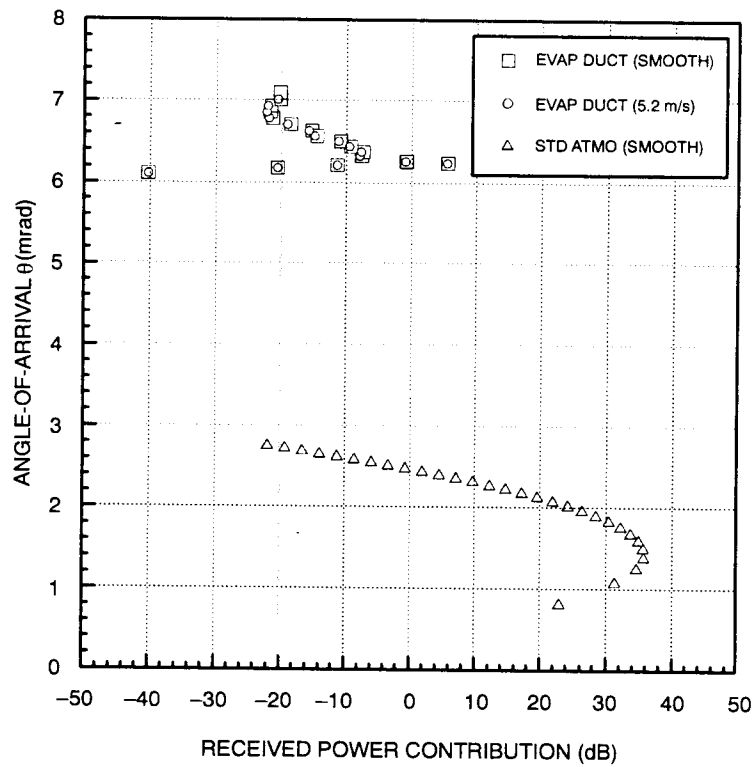


Figure 43. Estimated angle-of-arrival at 10.5 GHz for 1130 GMT on 21 September 1993.

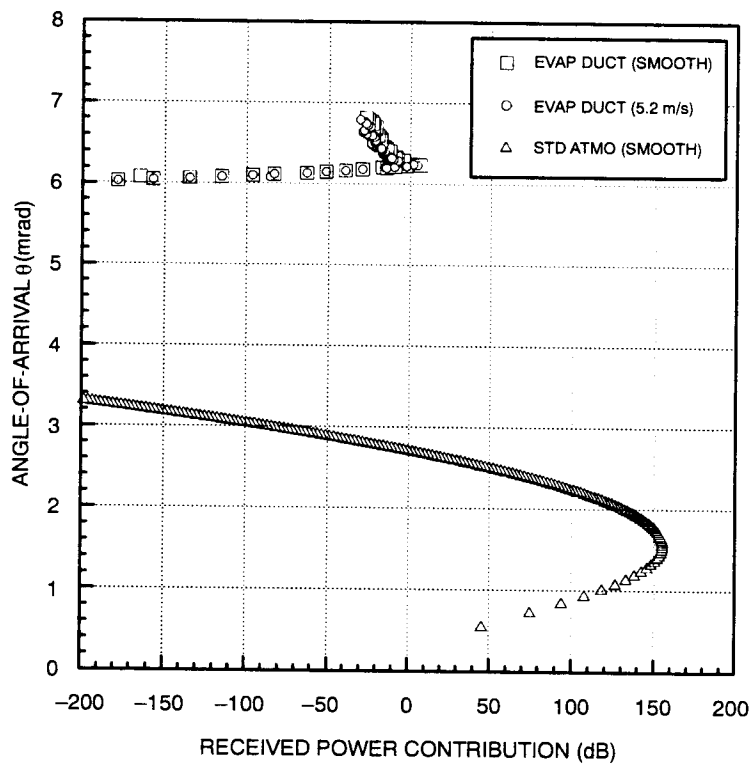


Figure 44. Estimated angle-of-arrival at 35 GHz for 1130 GMT on 21 September 1993.